Experimental study of the rare decays $K_L^0 \to \mu e$, $K_L^0 \to ee$, $K_L^0 \to \mu\mu$, and $K_L^0 \to eeee$

T. Akagi[1],[*] R. Fukuhisa,[2],[†] Y. Hemmi,[3] T. Inagaki,[4] K. Ishikawa,[2],[‡] T. Kishida,[2],[§] M. Kobayashi,[4]
T. K. Komatsubara,[2],[‖] M. Kuze,[2],[‖] F. Sai,[2],[†] T. Sato,[4] T. Shinkawa,[4] F. Suekane,[4],[¶] K. Takamatsu,[4]
J. Toyoura,[2],[**] S. S. Yamamoto,[2],[††] and Y. Yoshimura[4]

[1] Department of Physics, Tohoku University, Sendai 980, Japan
[2] Department of Physics, University of Tokyo, Tokyo 113, Japan
[3] Department of Physics, Kyoto University, Kyoto 606, Japan
[4] KEK, National Laboratory for High Energy Physics, Tsukuba 305, Japan

(Received 30 September 1994)

An experiment to search for the $K_L^0 \to \mu e$ and $K_L^0 \to ee$ decays and to measure the branching ratio of the $K_L^0 \to \mu\mu$ decay was performed at the KEK 12-GeV Proton Synchrotron. The single-event sensitivity of the present experiment for these channels was around 4×10^{-11}. No event was observed in the fiducial region for the $K_L^0 \to \mu e$ decay and one event, which could not be distinguished from the background, was observed in the fiducial region for the $K_L^0 \to ee$ decay. The obtained upper limits on the branching ratios at 90% confidence level were $B(K_L^0 \to \mu e) < 9.4 \times 10^{-11}$ and $B(K_L^0 \to ee) < 1.6 \times 10^{-10}$. The branching ratio of the $K_L^0 \to \mu\mu$ decay was obtained to be $[7.9 \pm 0.6(\text{stat})\pm 0.2(\text{syst})] \times 10^{-9}$ based on 179 events in the fiducial region. Using 18 events with the effective mass $M_{e^+e^-} > 470$ MeV/c^2 in the e^+e^- sample for the $K_L^0 \to ee$ decay search, the branching ratio of the $K_L^0 \to e^+e^-e^+e^-$ decay was estimated to be $[6 \pm 2(\text{stat})\pm 1(\text{syst})] \times 10^{-8}$ for $M_{e^+e^-} > 470$ MeV/c^2 and $[7 \pm 3(\text{stat})\pm 2(\text{syst})] \times 10^{-8}$ for $M_{e^+e^-} > 480$ MeV/c^2.

PACS number(s): 13.20.Eb

I. INTRODUCTION

The study of rare kaon decays has played important roles in the development of the standard model and has a bearing on the search for new interactions beyond the standard model. The lepton-flavor-changing process $K_L^0 \to \mu e$ is forbidden in the standard model and highly suppressed in the minimally extended model [1]. Therefore, it provides a good means to look for new interactions such as interactions among generations [2] and those given by the left-right symmetric model [1,3], the composite model [4] and the technicolor model [5]. The $K_L^0 \to ee$ and $K_L^0 \to \mu\mu$ decays are flavor-changing neutral-current processes which proceed through the second-order electroweak interaction. The former is much more suppressed than the latter due to the muon-electron mass difference, and its branching ratio is predicted to be $(3\text{--}5)\times 10^{-12}$ [6,7]. An observation of the $K_L^0 \to ee$ decay with the present sensitivity of

4×10^{-11} would imply the existence of a new interaction. For the branching ratio of the $K_L^0 \to \mu\mu$ decay there is a lower bound, the so-called unitarity limit with the value $B(K_L^0 \to \mu\mu) > (6.82 \pm 0.32) \times 10^{-9}$ [6,8], which was calculated from the measured branching ratio of the $K_L^0 \to \gamma\gamma$ decay, which is $(5.70 \pm 0.27) \times 10^{-4}$ [9]. If the measured branching ratio is smaller than the unitarity limit, it implies the existence of a new phenomenon. If it is greater than the unitarity limit, it indicates a pure weak contribution which constrains the values of the standard model parameters [10]. Since the deviation from the unitarity limit is expected to be very small, a very precise measurement of the branching ratio is necessary to detect it and to provide useful constraints on theory.

The experiment (KEK-E137) has been performed at the KEK 12-GeV Proton Synchrotron, using a K_L^0 beam line and a double-arm spectrometer which were designed and constructed for this experiment. The single-event sensitivity of the experiment for the branching ratios of the $K_L^0 \to \mu e$, ee, and $\mu\mu$ decays was about 4×10^{-11}. This is better than those previously achieved [11–13], and comparable to that of the recent experiment by the BNL-E791 Collaboration [14]. This paper presents a full description of the experimental procedures and results of KEK-E137 which have been partially published earlier [15].

II. EXPERIMENTAL SETUP

A. Beam line

The K_L^0 beam line consisted of four bending magnets ($B1$, $B2$, $B3$, and $B4$) to sweep away charged particles, two collimators to define a neutral beam profile and a

---

[*] Present address: Dept. of Phys., SLAC, Stanford, CA 94309.

[†] Present address: Tokyo Res. Lab., IBM Ltd., Yamato 242, Japan.

[‡] Present address: Wakamatsuhigashi, Okazaki 444, Japan.

[§] Present address: Rad. Lab., Riken, Wako 351-01, Japan.

[‖] Present address: INS (Univ. of Tokyo), Tanashi 188, Japan.

[¶] Present address: Dept. of Phys., Tohoku Univ., Sendai 980, Japan.

[**] Present address: Res. Lab., Mitsubishi Elec. Corp., Amagasaki 661, Japan.

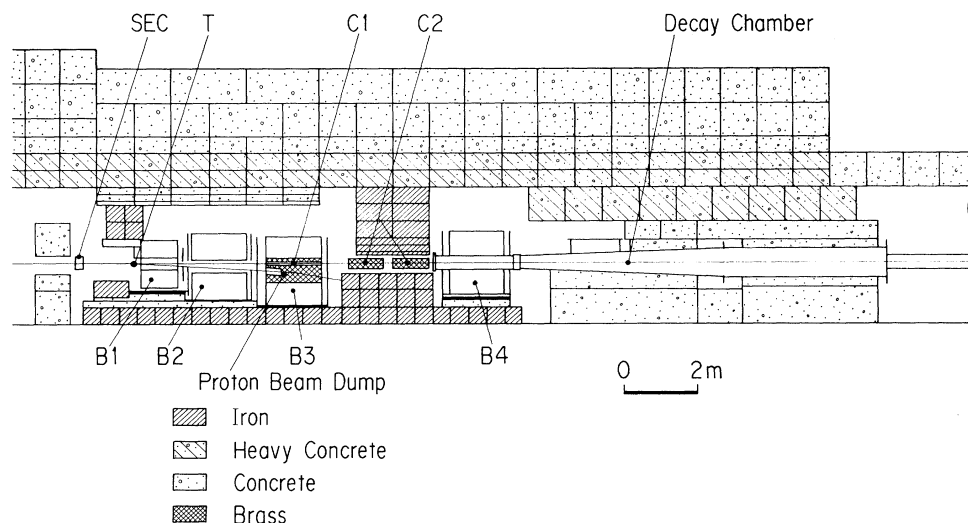[††] Present address: Dept. of Phys., Sophia Univ., Tokyo 102, Japan.

FIG. 1. Side view of the beam line and the decay chamber. SEC is a secondary emission chamber used as a beam intensity monitor. T and $B1$–$B4$ are the production target and the bending magnets, respectively. $C1$ and $C2$ are the first and second collimators. Primary protons were bent downward.

decay chamber as shown in Fig. 1. In order to obtain as many K_L^0 decays as possible the beam line had a large solid-angle acceptance at a small production angle and a long decay region. The primary protons with the momentum of 13 GeV/c hit a copper target (T) 12 cm long and 1 cm in diameter placed in front of $B1$. The primary beam intensity was monitored by a secondary emission chamber (SEC) located in front of the target. $B1$ and $B2$ bent the beam of straight-through protons downward and separated it from the neutral beam which was taken at $0°$ with respect to the primary beam. The bent proton beam was absorbed by a beam dump which was made of brass and tungsten and was placed in $B3$. The first collimator ($C1$) was fitted also in the pole gap of $B3$. It was made of brass and its inner wall at the front end was covered by tungsten. The aperture of the collimator was circular with a half-cone angle of 7 mrad with respect to the production target. The length of the collimator was 1.99 m. A pair of 1-m-long brass collimators, designated as the second collimator ($C2$), was placed between $B3$ and $B4$ to scrape the halo of the neutral beam. Each component of the second collimator had a circular aperture giving a half-cone angle of 9 mrad and was horizontally movable so that the effective aperture of the second collimator could be adjusted. The horizontal aperture of the second collimator was 8 mrad during the first three quarters of the running period. The pole gap of $B4$ was 30 cm which was large enough compared to the beam diameter of about 14 cm. The length of the beam line up to the downstream end of $B4$ was 10 m, which was long enough to reduce the presence of muons produced around the production target to a negligible level. The field strengths of magnets $B1$, $B2$, $B3$, and $B4$ were 2, 3, 3, and 2 Tm, respectively.

The neutral beam profile was measured during a beam survey at an early stage of the experiment. The beam profile of particles except for thermal neutrons was defined in such a way that the counting rate of a monitoring plastic scintillation counter per unit area in the

beam region was about 10^3 times that in the surrounding halo region. The flux of K_L^0's with momentum between 2 and 8 GeV/c was about 5×10^6, that of neutrons with energy greater than a few MeV $(0.7–2.2) \times 10^9$ and that of γ rays with energy greater than 100 MeV about 2.0×10^8 all at 10^{12} protons per pulse (ppp). No hot spot was observed in the detector area after closing the second collimator. The momentum spectrum of K_L^0's at the production target is shown in Fig. 2, which was obtained from the $K_L^0 \to \pi^+\pi^-$ events after correcting for the K_L^0 decay probability and the detector acceptance and efficiency. The shape of the spectrum was different from that obtained from averaging the K^+ and K^- yields using the Sanford-Wang formula [16], which is also shown in the figure.

The upstream end of a 10-m-long iron decay chamber started at 10.5 m from the K_L^0 production target. About 8% of K_L^0's with momenta between 2 and 8 GeV/c decayed in it. The neutral particles including the surviving K_L^0's were led to a secondary beam dump through a beam pipe. The beam pipe was connected to the decay chamber and passed through the middle of the detectors. It was made of thin aluminum with a structure like corrugated cardboard with an effective thickness of 5 mm. The beam pipe was tapered with a half-cone angle of 10 mrad with respect to the production target. The length of the pipe was 11 m and the inner diameter changed from 40 cm at the upstream end to 62 cm at the downstream end. The secondary beam dump was designed so as to obstruct particles which were backscattered toward the detectors. It was composed of paraffin plates, iron, and concrete blocks and aluminum plates impregnated boron 10% by weight. Three plastic scintillation counters were placed at the end of the beam pipe: one was placed at the center of the beam and the other two on both sides of the beam center 30 cm away from it. The counting rates of these counters were used to monitor the beam condition during the experiment.

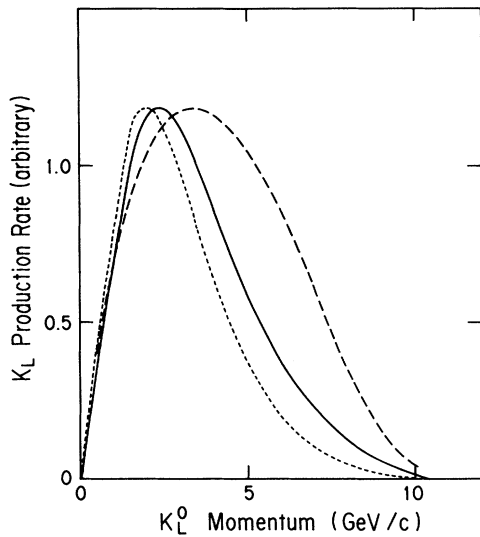The beam line was evacuated from the upstream end

FIG. 2. K_L^0 momentum spectrum at the production target obtained from the experimental data for $K_L^0 \to \pi^+\pi^-$ decay. The solid and dotted curves are the spectra for the production angle of $0°$ and $2°$, respectively. The dashed curve is the result of a calculation using the Sanford-Wang formula for $0°$ production. All spectra were normalized to have the same peak values.

of $B4$ to the secondary beam dump through the decay chamber. The vacuum was kept at a pressure of around 10 Pa, except for the first 10% of the running period when it was 100 Pa. The decay chamber had two exit windows located symmetrically on both sides of the beam line to let particles come out into the detector area. Each window had the dimensions of 1 m $(w) \times 0.8$ m (h) and was covered with a sheet of polyester film (7.1 mg/cm^2) supported by carbon cloth (60.8 mg/cm^2).

The following modifications to the beam line were made after about 3000 h of data taking which corre-

sponded to three-quarters of the running period. The production angle was changed from $0°$ to $2°$ by changing the incident angle of the primary proton beam with a pair of bending magnets in front of the production target. The second collimator was replaced by a 1-m-long fixed collimator with a half-cone angle of 8 mrad placed in the vacuum region which was extended in the upstream direction by 2 m. By these modifications the counting rates of the detectors were reduced by a factor of about 3 for the same primary proton intensity. Therefore, it was possible to increase the primary proton intensity. As a result the number of reconstructed events increased from 8 events/pulse at 1×10^{12} ppp to 16 events/pulse at 2.5×10^{12} ppp. The beam pulse had the repetition rate of 2.65 sec with the width of 500 msec.

B. Detection apparatus

Figure 3 shows a plan view of the detection apparatus which was a double-arm spectrometer with trigger counter hodoscopes and particle identification counters in each arm. The vacuum beam pipe described in the previous section passed between the two arms. The spectrometer comprised two magnets $(M1, M2)$ and five drift chambers $(W1-W5)$ in each arm. The spaces between the drift chambers were filled with helium bags. The various counters were placed behind the spectrometer to minimize multiple Coulomb scattering in the spectrometer region. They consisted of a pair of hodoscopes $(H1, H2)$ for triggering, a gas Cherenkov (GC) counter and an electromagnetic (EM) shower counter for electron identification and a muon (MU) identifier for each arm. All detectors were placed in a chamber enclosed by 1-m-thick concrete blocks, and most of the electronics modules were placed in a hut just outside this chamber. The temperatures in the chamber and the hut were kept constant to within a few degrees.
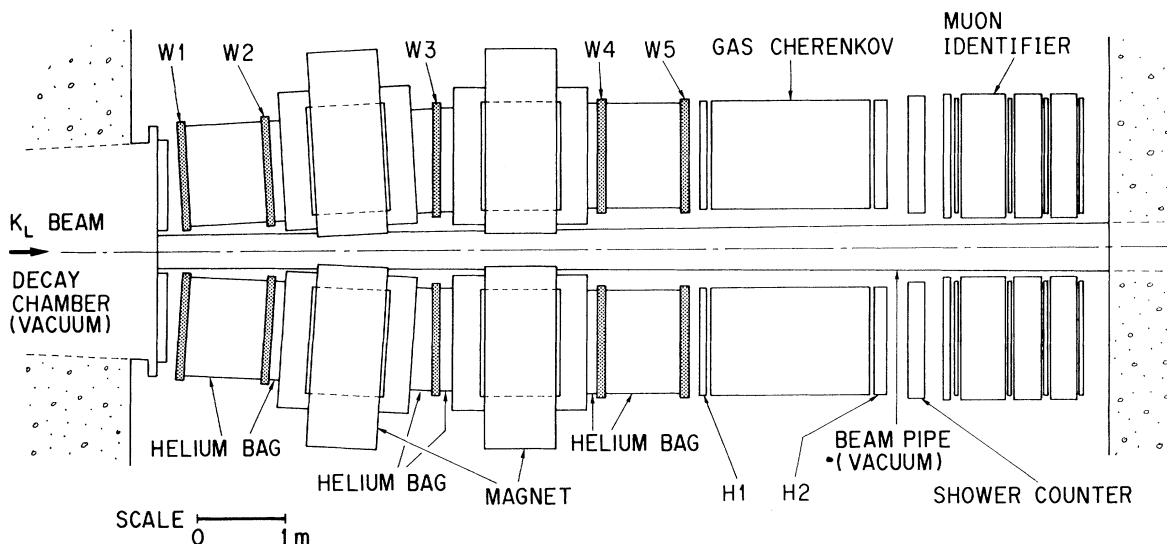

FIG. 3. Plan view of the detection apparatus.

1. Spectrometer magnets

The four magnets had the same size (100-cm pole gap, 130 cm wide and 80 cm long), and they were equally excited with the same polarity. The first magnet in each arm was placed at an angle of 3° with respect to a line perpendicular to the beam axis as shown in Fig. 3. The field strength at the center of each magnet was about 2.8 kG. The three components of the magnetic field were measured with an accuracy of less than 1 G in meshes of 5 or 2.5 cm in the x and y coordinates and 2.5 cm in the z coordinate over the spectrometer region. x, y, and z are the horizontal, vertical, and beam direction axes in the Cartesian coordinates. The field measurement was performed at the experimental site after setting up all detectors except for the drift chambers in order to obtain a field map including the distortion of the field due to the other iron structures. The bending field strength integrated along the track was adjusted to be 0.79 Tm in each arm and its distribution was flat over the acceptance as shown in Fig. 4. 0.79 Tm corresponded to a transverse momentum impulse of 238 MeV/c. Since the maximum transverse momenta of the secondary particles from the two-body decays of K_L^0 are 238, 249, 225, and 206 MeV/c for the $K_L^0 \to \mu e$, $\mu\mu$, and $\pi^+\pi^-$ decays, respectively, both secondary particles from nearly transverse two-body decays in the K_L^0 rest frame were emitted almost parallel to the beam axis after passing through the magnets. The magnetic field was monitored with a nuclear magnetic resonance (NMR) flux meter attached to a pole face of each magnet, and its variation was kept to within 0.03% during data taking.
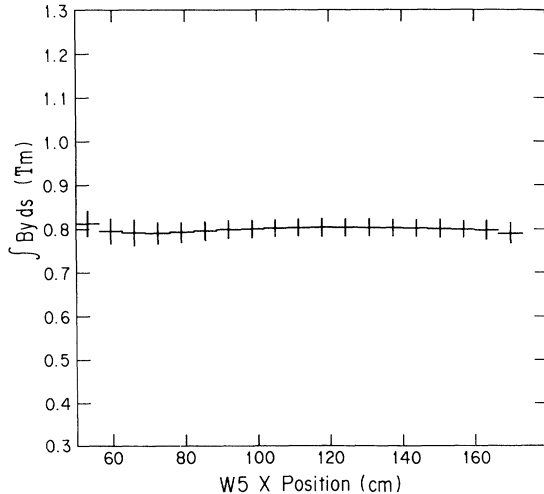

FIG. 4. Bending field strength integrated along tracks ($\int B_y ds$). The tracks were obtained from a Monte Carlo calculation for the $K_L^0 \to \mu e$ decay. The abscissa gives the horizontal position of the track at $W5$. The error bars represent the maximum variation of the integrated field strength due to various trajectories with various momenta from the decay points within the beam cone in the decay chamber.

2. Drift chambers

The five drift chambers ($W1$-$W5$) had the effective area of 115.2 cm (w) × 86.4 cm (h) ($W1$ and $W2$) and 115.2 cm (w) × 115.2 cm (h) ($W3$-$W5$). The distance between the beam axis and the innermost X wire was 30.5, 35.7, 49.7, and 54.7 cm for $W1$, $W2$, $W3$ and both $W4$ and $W5$, respectively. All chambers had the same structure. Each pair of drift chambers W_i in the left and right arms were placed on a single stand with the relative position accuracy of less than 0.1 mm. $W1$ and $W2$ were placed at an angle of 3° with respect to a line perpendicular to the beam axis in each arm. Each chamber consisted of four anode wire planes, $X(Y)$ and $X'(Y')$. The wire spacing in every plane was 9 mm with an accuracy of 50 μm. The $X(Y)$ and $X'(Y')$ wires were staggered by a half cell to resolve the left-right ambiguity. The number of anode wires in each plane was 128 except for that of the Y and Y' planes of $W1$ and $W2$, which was 96. The total number of anode wires was 4864. Each anode wire was surrounded by six cathode wires forming a hexagonal cell structure as shown in Fig. 5. Two guard wire planes whose wires were strung perpendicularly to the anode wires with the same spacing of 9 mm formed the outermost planes of the chamber. The anode wire was 20-μm gold-plated tungsten and the cathode and guard wires were 100-μm gold-plated aluminum. The tungsten and aluminum wires were strung with a tension of 40 and 80 g, respectively.

The drift chamber gas was a mixture of 50% argon and 50% ethane. The mixing ratio was kept constant to within 0.5% by mass flow meters. The cathode voltage was −2000 V for $W3$, $W4$, and $W5$. It was −1950 V for $W1$ and $W2$, which had higher counting rates than the others. The voltage supplied to the guard wires was −1.850 V to generate a symmetrical electric field inside the drift cell. The voltage supplied to the guard wires was lower than that to the cathode wires to prevent electrons made outside the drift cell from entering it. The material in each drift chamber was 1.08×10^{-3} radiation lengths. The helium bags between the drift chambers were made of double layers of polyethylene sheet and one
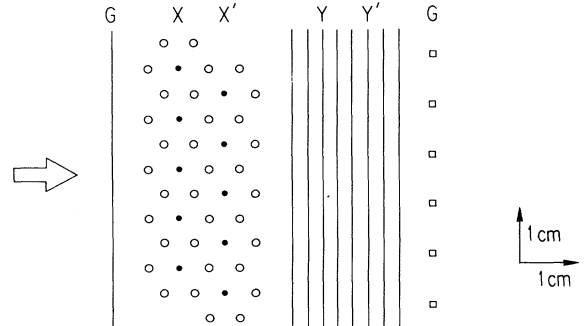

FIG. 5. Schematic view of the cell structure of the drift chamber. The dots, open circles, and squares show the anode, cathode, and guard wires strung perpendicular to the plane of the figure, respectively. The wires strung parallel to the plane are shown by the solid lines. Particles come in the direction of the arrow.

layer of aluminized polyester sheet with the total thickness of 35 μm. The helium content in the bags was kept constant to better than 99%, which was checked by a gas chromatograph. The total radiation length of each arm of the spectrometer (up to $W5$) was 1.0×10^{-2}, including the window of the decay chamber.

16-channel preamplifiers attached to the drift chambers amplified the anode signals with a gain of 12.5 mV/μA. These signals were further amplified by 32-channel amplifier-discriminators by a factor of 10 and shaped into ECL (emitter coupled logic) signals. The threshold of the discriminator was set at around 90 mV. The ECL signals were sent via 30-m twisted pair cables to 32-channel drift chamber TDC (time-to-digital converter) modules in TKO (Tristan KEK Online-system) crates [17] which are standard crates at KEK. Each module included 32 chips of 300-nsec delay and time-to-amplitude converter and a set of a multiplexer and an ADC (amplitude-to-digital converter). The drift chamber signal was gated with a 175-nsec width signal which was produced by the master trigger. The time difference between the drift chamber signal and the delayed master trigger was AD converted. The time resolution of the TDC was 700 psec and the conversion time was 12 μsec

FIG. 7. K_L^0 momentum dependence of the effective mass resolution for the $K_L^0 \to \pi^+\pi^-$ decay.

per hit. $W1$ had the highest counting rate, and the maximum counting rate was about 60 MHz at the primary proton intensity of 1.5×10^{12} ppp for 0° production. The maximum single-wire counting rate was 0.9 MHz.

The TDC was calibrated from time to time by feeding signals from a pulse generator to each signal line. The relative position of the drift chamber was calibrated by using straight tracks in runs with the magnets turned off. The drift velocity was parametrized with a cubic spline function of the drift time. The parameters were calibrated by an iterative method using real tracks in regular runs. The spatial resolution was estimated from the deviation of the sum of the drift lengths of a pair of hits in the staggered planes from a half cell size of 4.5 mm. It was 330 μm for $W1$ and $W2$ and 280 μm for $W3$, $W4$, and $W5$. These values were used for the track χ^2 analysis and Monte Carlo calculations to be described later. Figures 6(a) and 6(b) show the efficiencies of planes X and X' of drift chamber $W2$ at various voltages supplied to the cathode and guard wires. The obtained spatial resolutions were also shown in Fig. 6(a). At 2100 V the resolution reached 190 μm.

The track momentum (P) resolution of the spectrometer was estimated by a Monte Carlo calculation to be

$$\sigma(P)/P = \sqrt{0.019[P(\text{GeV}/c)]^2 + 0.11}\% \ .$$

The calculated effective $\pi^+\pi^-$ mass resolution for the $K_L^0 \to \pi^+\pi^-$ decay is shown in Fig. 7 as a function of K_L^0 momentum. It does not show much dependence on the K_L^0 momentum.
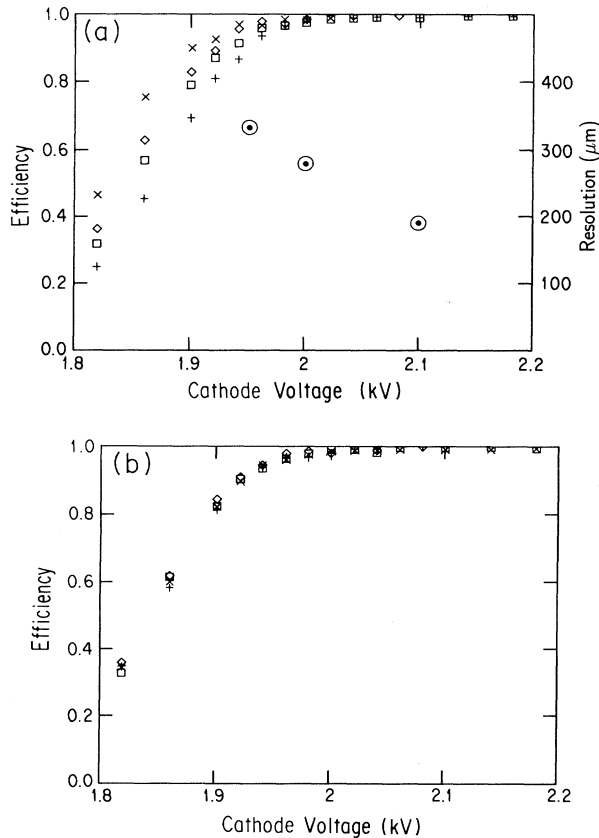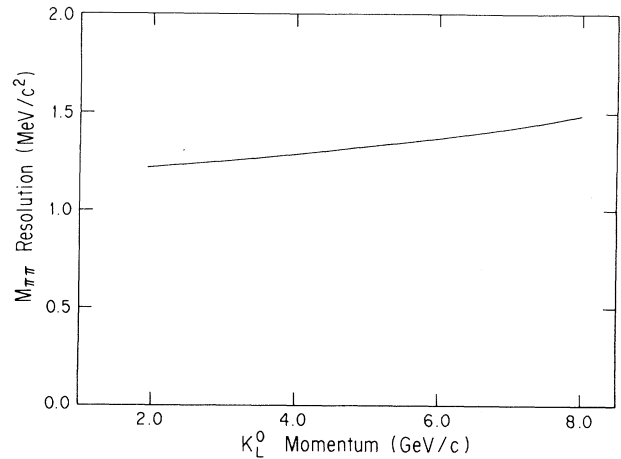

FIG. 6. Dependences of the efficiencies on the high voltage supplied to the cathode wires for (a) the X and (b) the X' planes of the drift chamber $W2$ at various voltages for the guard wires, 2.00 kV ($\times$), 1.85 kV ($\Diamond$), 1.70 kV ($\Box$), and 1.55 kV ($+$). $\odot$ in (a) indicates the spatial resolution measured at the guard wire voltage of 1.85 kV.

3. Hodoscopes

A pair of hodoscopes, $H1$ and $H2$ separated by a distance of 2 m, were placed behind $W5$. They were used for making the reference signal for timings as well as the basic trigger which required at least one secondary charged particle in each arm which was nearly parallel to the
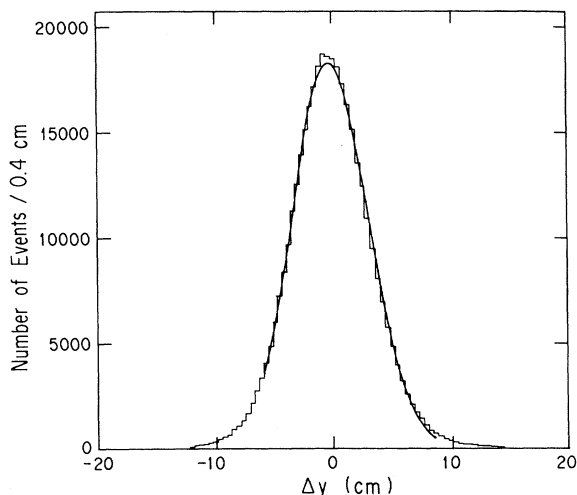
FIG. 8. Distribution of the vertical position obtained from the time difference between the top and bottom photomultiplier signals of an $H1$ counter with respect to the track position. The solid line is a Gaussian distribution with the standard deviation of 3.2 cm.

beam direction. Each hodoscope consisted of 16 vertical plastic scintillation counters, the dimensions of which were 7 cm (w) × 116 cm (l) × 1 cm (t) for $H1$, and 12 cm (w) × 140 cm (l) × 1 cm (t) for $H2$. The counters of both hodoscopes were arranged by a center-to-center spacing of 7.2 cm. There was a 2-mm gap between counters of $H1$, and the adjacent counters of $H2$ overlapped each other by 4.8 cm. The center of each $H2$ counter was located at the same horizontal position as that of the corresponding $H1$ counter. A corresponding pair of $H1$ and $H2$ counters covered an angular divergence of at least ±12.5 mrad which was enough to cover the divergence of the K_L^0 beam. Each counter was viewed from the top and bottom ends by 2-in. photomultipliers, and both signals were discriminated and inputted to TDC's and a mean timer. The relative timings among the counters in each hodoscope were adjusted to within 0.5 nsec of each other by a calibration run in which a horizontal scintillation counter covering all 16 hodoscope counters was placed in front of the hodoscope. The time difference between the signals from the top and bottom photomultipliers of $H1$ gave the vertical position information of the track with a spatial resolution of 3.2 cm as shown in Fig. 8. This position information in the vertical direction was used in the track reconstruction.

4. Electron identifiers

Electrons were identified by a gas Cherenkov counter and an electromagnetic shower counter. The gas Cherenkov counter was placed between $H1$ and $H2$ in each arm. The Cherenkov radiator was air at atmospheric pressure with refractive index of 1.000 273. The threshold momentum for muons was 4.5 GeV/c. The Cherenkov light was focused onto four 5 in. photomulti-

pliers by four curved mirrors. The effective length of the radiator was 1.5 m. The trigger threshold for electrons was set at the one photoelectron level.

The second electron identifier, the electromagnetic shower counter, was located just behind $H2$. It consisted of 16 vertically arranged modules. Each module was made up of ten alternate layers of iron or lead and plastic scintillator with the dimensions of 8 cm (w) × 152 cm (h). The first layer was a 12-mm-thick iron plate followed by a 6-mm-thick scintillator, and each of the other nine layers was an 8-mm-thick lead plate followed by a 6-mm-thick scintillator. The lead plates included 8% antimony by weight. To observe the shower development, each module was divided into two sections. The forward section consisted of the first four layers and the backward section the last six layers. The forward section had 5.0 radiation lengths and the backward one 8.7 radiation lengths. Each section was viewed by 2-in. photomultipliers at the top and bottom ends. The energy deposition above 500 MeV was required for the electron trigger for the 0° production run.

5. Muon identifier

The muon identifier consisted of four iron blocks each of which was followed by a plastic scintillation counter array (MU1–MU4). The dimensions of the blocks were 152 cm wide and 190 cm high with thicknesses of 10, 50, 30, and 30 cm from the upstream end. The minimum momenta of muons which could penetrate these iron blocks were 0.4, 1.0, 1.4, and 1.8 GeV/c taking into consideration the upstream material such as the shower counter. Both MU1 and MU2 were composed of six vertical scintillation counters with the dimensions of 22 cm (w) × 162 cm (l) × 1 cm (t), and each counter was viewed from both the top and bottom ends by 2-in. photomultipliers. Both MU3 and MU4 were made up of eight horizontal counters with the dimensions 21 cm (w) × 140 cm (l) × 1 cm (t), and each counter was viewed from one side by a 2-in. photomultiplier. The muon trigger required a coincidence between a pulse from an MU1 counter and the one from the corresponding MU2 counter or its adjacent counters. This was equivalent to requiring the muon momentum to be above 1 GeV/c.

C. Trigger and data taking

Two basic triggers were formed with hodoscopes $H1$ and $H2$. One was a "parallel" trigger for the $K_L^0 \to \mu e$, ee, and $\mu\mu$ decays and the other a "semiparallel" trigger for the $K_L^0 \to \pi^+\pi^-$ decay. The parallel trigger required a coincidence between one $H1$ counter and the corresponding $H2$ counter in both arms. In the $K_L^0 \to \pi^+\pi^-$ decay the pions have a lower maximum transverse momentum than the leptons in the leptonic two-body decays and will be bent a little inward by the spectrometer magnets. Therefore, in order to detect these pions the semiparallel trigger was formed by adding to the parallel coincidence a coincidence between an $H1$ counter and

the $H2$ counter adjacent to the corresponding $H2$ counter on the beam pipe side in each arm. These parallel and semiparallel requirements reduced the acceptance for the three- and four-body decays without a large reduction in the acceptance for the two-body decays.

A coincidence between both electron identifiers was required for an electron track and a signal from the muon identifier was required for a muon track in addition to the parallel trigger. The $K_L^0 \to \pi^+\pi^-$ decay was triggered by the semiparallel requirement only, and the data collected by this $\pi^+\pi^-$ trigger contained events from the $K_L^0 \to \pi e\nu$ (K_{e3}) and $K_L^0 \to \pi\mu\nu$ ($K_{\mu3}$) decays. This trigger was scaled down by a factor of about 500 with a preset scaler. No anticoincidence was required in any trigger. The data for all four decays were simultaneously collected.

A block diagram of the data taking system is shown in Fig. 9. The trigger signal inhibited the subsequent trigger and started the conversion process of TDC in ten TKO crates for the drift chambers and TDC and ADC in six CAMAC crates for the counters. The seventh CAMAC crate was used for the scalers to count the hits in various counters. If an event had no hit on either plane of any staggered pair of any one of the drift chambers, the conversion process was stopped and all TDC and ADC modules were cleared. The decision time for this hardware filtering of events was 750 nsec and the clearing process took 12 μsec. Otherwise, the trigger signal was delayed 60 μsec for the conversion and was used as a scan start signal to the 16 memory modules. Each memory module scanned the data in all TDC and ADC modules in the crate connected to it. In the scanning process TDC channels without a signal and ADC channels without a signal above the pedestal were skipped. After transferring the data to the memory modules, all TDC and ADC modules were cleared and enabled to accept the subsequent trigger. The average transfer time including the conversion and clearing times was around 200 μsec/event. The dead time, which resulted from the inhibition of the subsequent trigger during this transfer time or the time for filtering events with unsatisfactory chamber hits, was around 5% of the entire data acquisi-

tion time. Each memory module had 32 kbytes. During a beam-off period of about 2 sec, the counts in the scalers were read out and all data in the 17 memory modules were serially transferred to an online computer, μ vax II. The timing of the trigger with respect to the accelerator clock was also recorded.

In the on-line computer the data whose timing difference between the $H1$ signals in the left and right arms exceeded by more than 5 nsec were discarded. The rejection rate by this criterion was around 20% under the normal running condition. The accepted data were written on magnetic tape before the arrival of the next beam pulse. The number of triggers per beam pulse was around 120 under the normal running condition. The values of several important scalers were averaged over several pulses, converted to analog level signals and inputted to a pen recorder. This was very important for monitoring the running condition.

Several special runs were performed at least once every two weeks. Those were a run randomly triggered by a pulse generator signal under various beam conditions, a magnet-off run and a minimum bias runs in which only energy deposit in the shower counters in both arms was required. After a half year of detector tuning the data taking started in June 1988 with 0° production. The average primary proton intensity was about 1.3×10^{12} ppp. In the summer of 1989 the beam condition was changed to 2° production. Using an increased intensity of 2.0×10^{12} ppp, the data taking continued up to May 1990. We accumulated a total of 3.2×10^8 events by the μe, ee, and $\mu\mu$ triggers and 0.8×10^8 events by the prescaled $\pi^+\pi^-$ trigger. The off-line data analysis was done by a HITAC M280/680 computer.

III. DATA ANALYSIS

A. Track finding and first track fitting

The tracks were reconstructed with the information from the hodoscopes and drift chambers. First, we searched for $H1$ hit pairs in the left and right arms whose mean-timer outputs were within 3 nsec of one another and set the trigger timing. The resolution of this timing was 0.62 nsec. Then drift chamber hits which were within an interval between -20 and 130 nsec with respect to the trigger timing were selected. In each arm $H1$ hits with the corresponding $H2$ hits satisfying the semiparallel condition were searched for. Roads were then defined by connecting the hodoscope hits with the beam profile in the decay chamber in each of the vertical and horizontal planes. The $H1$ top/bottom time difference was used as the vertical coordinate. By requiring at least one hit in the staggered planes in each coordinate of each drift chamber within each road, the number of roads was efficiently reduced. The number of hit candidates for further analysis was reduced by restricting the search to within the roads.

The track finding started from the most downstream drift chamber $W5$ and moved to the upstream chambers because the hit multiplicity was lower in the downstream
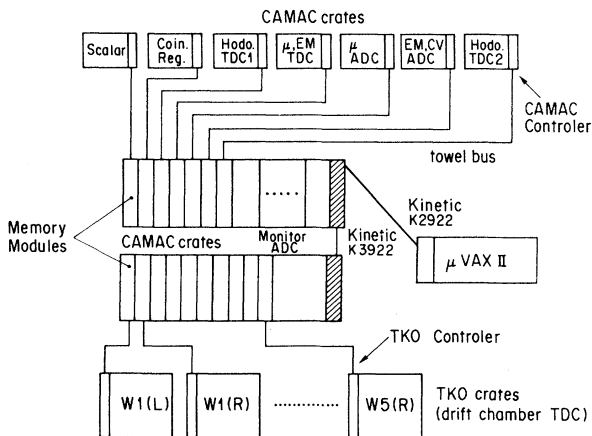

FIG. 9. Block diagram of the data acquisition system.

chambers. At this stage the particle trajectory was assumed to consist of three straight segments deflected through an equal angle at the centers of two magnets in the horizontal plane. It was assumed to be straight in the vertical plane. Hit candidates in each track were selected with the least-squares method. A track in each plane was required to have three or more drift chambers with paired hits in the staggered planes. Event candidates were reconstructed by pairing track candidates in both planes of both arms.

The track momentum was calculated from the sum of the deflection angles by assuming that the transverse momentum given by the spectrometer magnets was 238 MeV/c. The decay vertex was defined as the midpoint between the points of closest approach of the two tracks. The collinearity angle θ, which was defined as the angle between the momentum sum vector of the two particles and the target-to-vertex direction, was calculated. To reduce the background from the three-body decays, $P\theta^2$ was required to be less than 0.55 (MeV/c) rad^2, where P was the momentum sum of the two particles. The reason for using $P\theta^2$ was that this value should be zero for the two-body decays and that its resolution was not much dependent on the K_L^0 momentum. Furthermore, the effective mass of the two particles was required to be greater than 430 MeV/c^2 for the μe and $\mu\mu$ triggers. These cuts at an early stage of the tracking process were made to reduce the processing time. The effect of the cuts on the true events was studied using the $K_L^0 \to \pi^+\pi^-$ sample without the cuts and found to be negligibly small.

These surviving track candidates were fitted by the quintic spline method [18] to reconstruct particle tracks more precisely in each arm. The position (x_i, y_i) on the ith plane at z_i was expressed as

$$x_i = a_1 + a_2 z_i + \frac{1}{P} X(z_i) ,$$

$$y_i = b_1 + b_2 z_i + \frac{1}{P} Y(z_i) ,$$

$$\qquad (1)$$

where $X(z_i)$ and $Y(z_i)$ were derived by the double integration of the cubic spline expressions and represented the particle trajectory with the momentum P in the magnetic field in the x-z (horizontal) and y-z (vertical) planes, respectively. The index i covers the 46 planes along the trajectory between $W1$ and $W5$ including 20 drift chamber planes. Three components of the magnetic field were given at the track position in each of the 46 planes. They were calculated event by event by interpolating the magnetic field values given at mesh points in each plane.

The drift time was corrected for the propagation delay depending on the distance between the hit point and the preamplifier along the anode wire. It was converted to the drift length by using the calibration constants given for each anode wire. The left-right ambiguity for a pair of hits in the staggered planes was resolved by selecting the combination in which the derivative direction of the pair was closest to the track direction determined in the previous process. For a single hit along the track in the

staggered planes the hit position was assigned to be the hit anode-wire position.

The fitting was iterated four times, and an event candidate with a minimum value of the following χ^2 was selected:

$$\chi^2 = \frac{1}{f} \left(\sum_{L,R} \sum_{i=1}^{N_{L,R}} \frac{(X_i - x_i)^2}{\sigma_i^2} + \frac{\Delta d_v^2}{\sigma_v^2} \right) , \qquad (2)$$

where X_i was the measured position, x_i the fitted value, σ_i the spatial resolution which was 400 μm for the pair hits and 3.5 mm for single hits, Δd_v the closest distance between two tracks, and σ_v was the vertex resolution which was 1 cm. $N_{L,R}$, the total number of x and y planes with hits out of 20 planes in the left or right arm and $f = N_L + N_R - 10$, was the degree of freedom.

For the μe and $\mu\mu$ triggers the effective mass of the two particles was calculated again and it was required to be greater than 475 MeV/c^2 to reduce the background from the three-body decays.

The numbers of events which passed the track finding and first fitting processes were 1.7×10^6, 6.4×10^6, 0.73×10^6, and 6.9×10^6 for μe, ee, $\mu\mu$, and $\pi\pi$ triggers, respectively. The track parameters were recorded on magnetic tape together with the raw data information for the second track fitting.

B. Second track fitting

Based on the track candidates obtained above the second fitting including another hit search was carried out in order to calculate the track χ^2 more reliably. One of the causes which deteriorated the χ^2 values was an accidental hit just above a pair of hits on the staggered planes. In this case the accidental hit often changed the drift time information of one of the pair hits thereby causing a track to have a zigzag pattern. A fit to such a pattern increased the track χ^2. The second hit search was carried out within the space twice the sense wire spacing around the track previously obtained. For the pair in the staggered planes the sum of the drift distances was checked to see it was equal to the maximum drift length of 4.5 mm within three times its resolution after correcting for the incident angle of the track with respect to the chamber plane. For the pair not meeting this criterion the candidate was changed to a single hit by taking only the hit closest to the track. For the single hit the left-right ambiguity was resolved by taking the side closest to the track. The same spline fitting as before was performed using the new hit candidates. The spatial resolution of 400 μm was assigned to staggered hit wires and that of 0.1 cm was assigned to single-hit wires. The process including the hit search was also iteratively performed four times, and the best combination of the hit candidates was selected. We required at least 8 and 7 hits out of 10 in the x and y coordinates, respectively. Furthermore, we required that there should not be successive single-hit chambers in the x coordinate.

We recalculated the track χ^2 by the following equation using the error matrix for the spectrometer [19]:
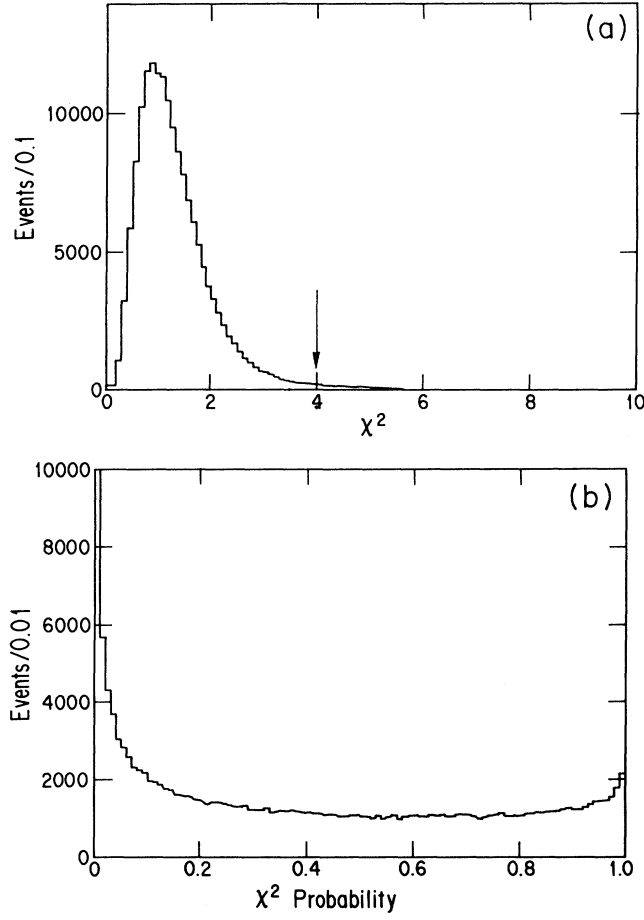
FIG. 10. (a) Distribution of the track χ^2 for the pion tracks in the left arm from the $K^0_L \to \pi^+\pi^-$ decay and (b) distribution of the χ^2 probability for the same track sample.

$$\chi^2 = \frac{1}{f}\left(\sum_{i=1}^{N}\sum_{j=1}^{N}(X_i - x_i)E_{ij}^{-1}(X_j - x_j)\right), \qquad (3)$$

where E_{ij} represented the error matrix, N was the total number of x and y planes with hits out of 20 planes, and $f = N - 5$ was the degree of freedom. The error matrix was divided into two parts;

$$E_{i,j} = \sigma_i^2 \delta_{i,j} + E_{i,j}^{MC}(P), \qquad (4)$$

where σ_i represented the measured position resolution of the ith plane of the drift chamber which was 300 μm for $W1$ and $W2$ and 280 μm $W3$ to $W5$. $E_{i,j}^{MC}$ represented the error correlation between the ith and jth planes due to multiple Coulomb scattering, and it was determined by a Monte Carlo calculation. Figures 10(a) and 10(b) show the distributions of the track χ^2 and the χ^2 probability for the pion tracks from the $K^0_L \to \pi^+\pi^-$ decay.

C. Track quality cuts

The cutoff value of the track χ^2 was chosen to be 4 for each arm. It was still loose enough so that only 0.5% of

the pion tracks from the $K^0_L \to \pi^+\pi^-$ decay were lost by this cut.

Track fitting was also carried out separately in the upstream and downstream halves of the spectrometer in each arm. The consistency of the two measurements was checked by using

$$\Delta_{UD} = (|P_U - P| + |P_D - P|)/P, \qquad (5)$$

where P was the momentum obtained with all chambers, P_U that with the upstream drift chambers $W1$, $W2$, and $W3$ only, and P_D that with the downstream drift chambers $W3$, $W4$, and $W5$ only. When a pion decayed in the spectrometer the Δ_{UD} would be different from zero, and requiring it to be close to zero reduced the background for the $K^0_L \to \mu e$ and $\mu\mu$ decays from the $K^0_L \to \pi e\nu$ and $\pi\mu\nu$ decays. Figure 11 shows the Δ_{UD} distribution for the genuine pion tracks from the $K^0_L \to \pi^+\pi^-$ decay. The cutoff value for Δ_{UD} was set at 0.06. The fraction of the loss due to this cut was about 7%. Figure 12 shows a scatter plot of the effective mass vs the collinearity angle squared for the $\mu\mu$ events for the case with a loose Δ_{UD} cut of 0.2. Comparing it with Fig. 45, the effectiveness of this cut to remove the background around the signal region is clearly seen.

Although the Δ_{UD} cut was important to reduce the serious background for the processes concerned, the cut might cause some systematic errors in the measurement of the branching ratios. Since the present measurement of the branching ratios of the decays $K^0_L \to \mu e$, $\mu\mu$, and ee was a ratio measurement with respect to the $K^0_L \to \pi^+\pi^-$ decay, the effect of this cut would appear in terms of the ratio of muon and electron tracks to pion tracks which survived the cut. Therefore, we studied this effect by using large μ, e, and π samples from the K_{l3} decay which were simultaneously collected by the $\pi^+\pi^-$ trigger. Figures 13(a)–13(c) show the momentum spectra of the pion, muon, and electron samples from the K_{l3} decays together with those obtained from Monte Carlo calculations. The pion spectrum which was obtained from the K_{e3} decay and used for the calibration is quite simi-
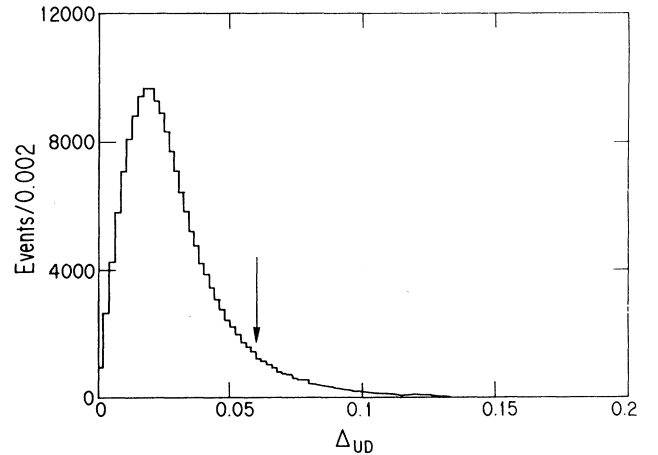

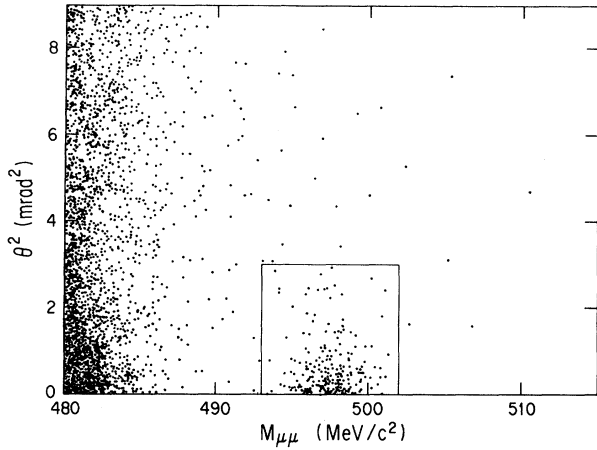FIG. 11. Δ_{UD} distribution of the pion track in the left arm from the $K^0_L \to \pi^+\pi^-$ decay.

FIG. 12. Scatter plot of the $M_{\mu\mu}$ vs θ^2 for the $\mu\mu$ events after all selection cuts except for the Δ_{UD} cut of 0.2 instead of 0.06.

lar to that obtained from the $K_L^0 \to \pi^+\pi^-$ decay shown in Fig. 18 in the next section. The spectra of muons and electrons used for the calibration are also similar to those obtained from the Monte Carlo generated leptonic two-body decays. Using these samples a double ratio $(\eta_{\mu,e}/\eta_\pi)_{\rm data}/(\eta_{\mu,e}/\eta_\pi)_{\rm MC}$ was calculated for various values of Δ_{UD} cut. η is the ratio of the number of tracks remaining after the cut to the number of tracks before the cut (no cut). Some cut had to be imposed on the real data even for the "no cut" case due to the background, and we estimated the "no cut" numbers by taking the cut value to be 0.20 which was far enough away from the actually applied value of 0.06. Figures 14(a) and 14(b) show the distributions of the double ratio $(\eta_\mu/\eta_\pi)_{\rm data}/(\eta_\mu/\eta_\pi)_{\rm MC}$ and $(\eta_e/\eta_\pi)_{\rm data}/(\eta_e/\eta_\pi)_{\rm MC}$ for various Δ_{UD} cut values. The errors are statistical. At $\Delta_{UD} = 0.6$ the corrections for muon tracks were 1.000 ± 0.004 and 1.003 ± 0.004 for the left and right arms, respectively, and those for electron tracks 0.980 ± 0.003 and 0.982 ± 0.003.

For the selected tracks the fiducial cuts at the vacuum window, the entrance to the first spectrometer magnet and the exit from the second magnet were applied. These additional cuts clearly defined the geometrical acceptance for the tracks, but they were loose enough to pass more than 99% of the $K_L^0 \to \pi^+\pi^-$ events before them.

D. Event selection

The following criteria were used to select the final events from the reconstructed events. In all figures in this section the histograms with the solid lines represent the distributions of the real $K_L^0 \to \pi^+\pi^-$ events, the symbol "+" represents the Monte Carlo results, and the cut-off values are indicated by the arrows.

(1) The distribution of the distance of the closest approach of two tracks in the opposite arms ($D_{\rm vertex}$) is shown in Fig. 15. The cut was effective to eliminate the background coming from the $K_L^0 \to \pi e \nu$ or $K_L^0 \to \pi\mu\nu$ decays followed by the decay $\pi \to \mu\nu$ in the decay cham-

ber. The resolution for the real data was slightly worse than that for the Monte Carlo result. One of the sources of this fact was the stray magnetic field extending out into the decay chamber which was not considered in the
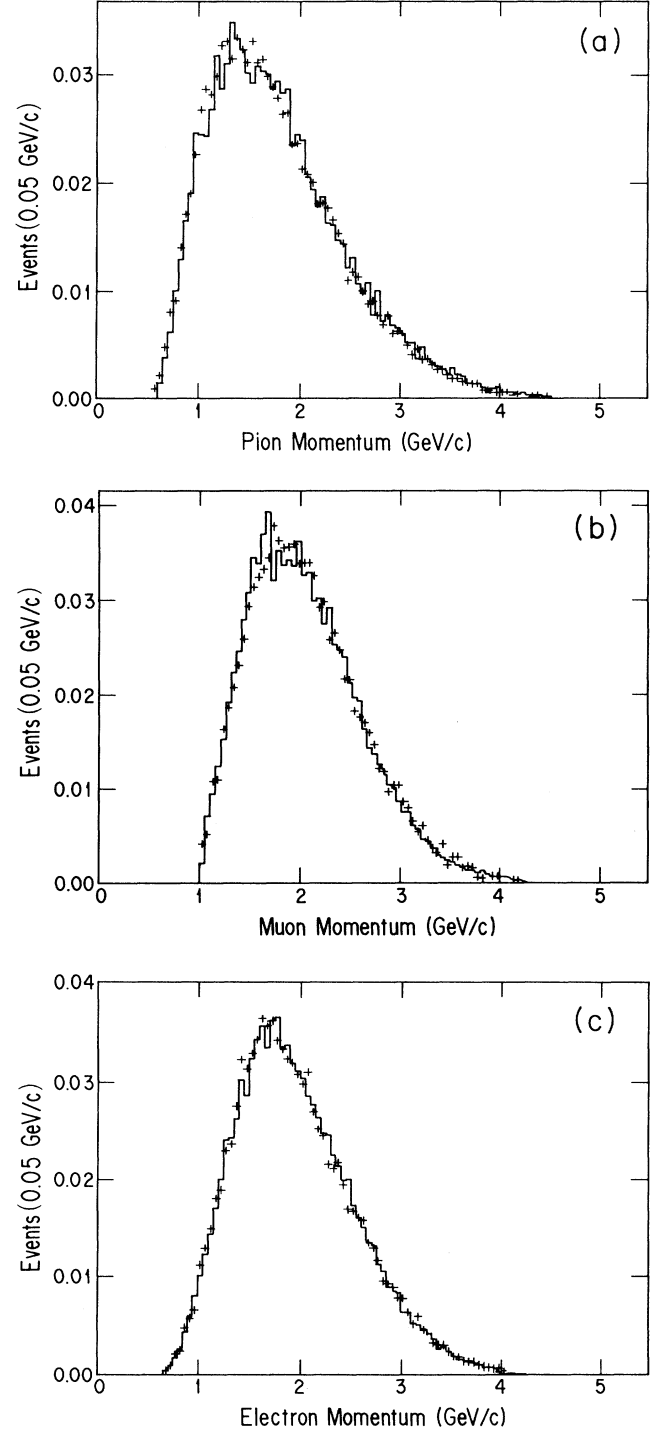

FIG. 13. Momentum spectra of (a) pion, (b) muon, and (c) electron samples from the K_{l3} decays, where the numbers of events was normalized to 1. The + indicates the Monte Carlo results.
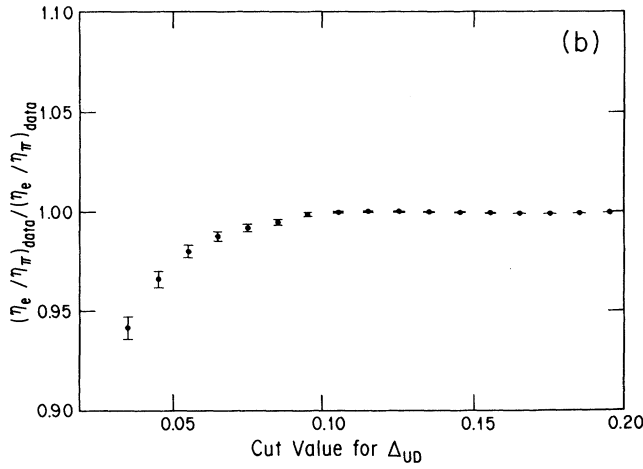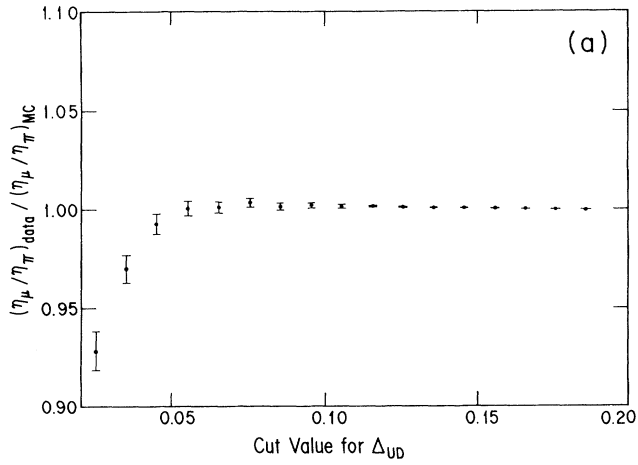
FIG. 14. Dependences of the double ratios (a) $[(\eta_\mu/\eta_\pi)_{\mathrm{data}}/(\eta_\mu/\eta_\pi)_{\mathrm{MC}}]$ and (b) $[(\eta_e/\eta_\pi)_{\mathrm{data}}/(\eta_e/\eta_\pi)_{\mathrm{MC}}]$ on the value of the Δ_{UD} cut.
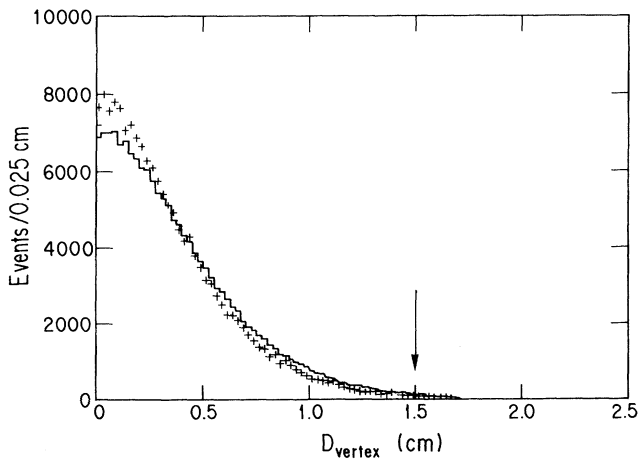
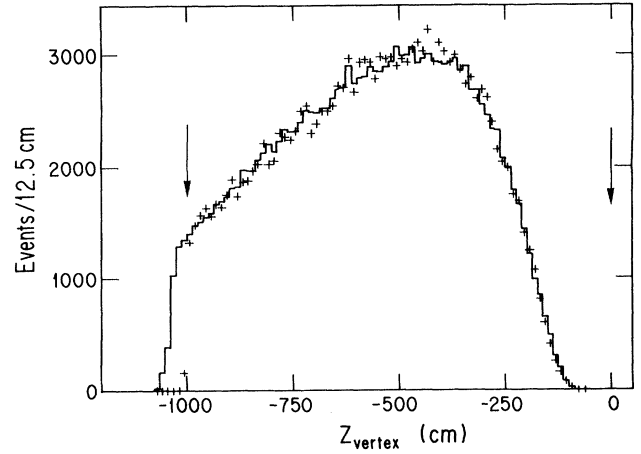FIG. 15. Distribution of the distance of the closest approach (D_{vertex}) of the two tracks.

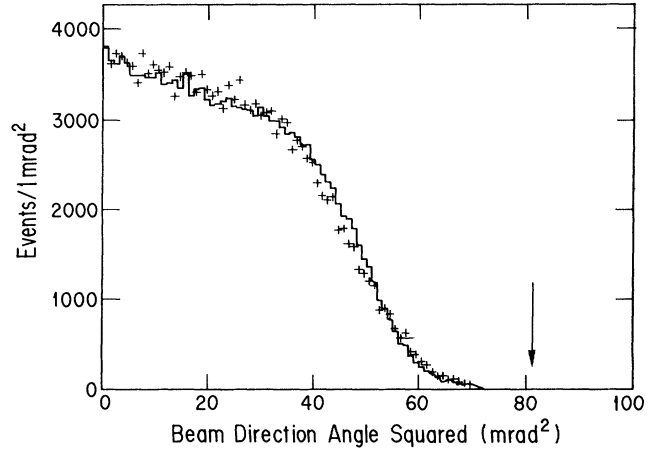FIG. 16. Distribution of the vertex position along the beam axis (Z_{vertex}).

FIG. 17. Distribution of the beam direction angle squared. The angle was defined as an angle between the vertex-to-target direction and the beam axis.
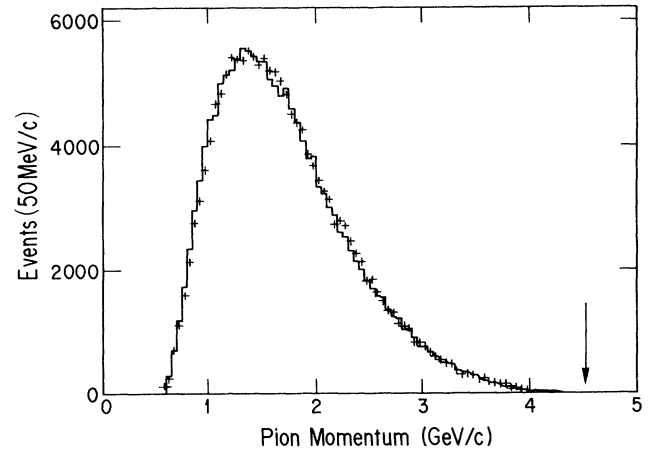
FIG. 18. Distribution of the pion momentum in the left arm.
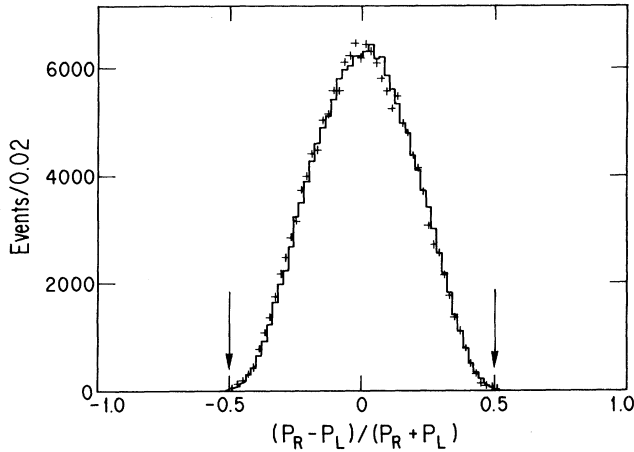
FIG. 19. Distribution of the momentum balance $(P_L - P_R)/(P_L + P_R)$ in the left and right arms.

present track fitting.

(2) The decay vertex position distribution along the beam axis (Z_{vertex}) and its fiducial boundaries are shown in Fig. 16. The upstream limit of -10 m, which was 50 cm away from the downstream pole face of the last beam line magnet $B4$, was chosen to avoid its fringe field effect.

(3) While the K_L^0 beam was collimated into a half-cone angle of 7 mrad with respect to the production target, the vertex should be within 9 mrad taking account of smearing due to the finite size of the production target and the resolution of the vertex position. Figure 17 shows the distribution of the square of the angle between the target-to-vertex direction and the beam axis.

(4) The particle momentum was required to be less than 4.5 GeV/c which is the threshold momentum of the gas Cherenkov counter for muons. The momentum distribution of pions from the $K_L^0 \to \pi^+\pi^-$ decay is shown in Fig. 18.

(5) The distribution of the momentum balance $(P_R - P_L)/(P_R + P_L)$ is shown in Fig. 19, where P_L and P_R are the momenta of the tracks in the left and right arms, respectively. The cutoff values of ± 0.5 were adopted.

These selection criteria were the same for all decay modes. The Monte Carlo calculations confirmed that the cuts were loose enough to pass more than 99% of genuine events for all decay modes.

E. Particle identification

1. π, e, and μ samples

The π, e, and μ samples from the K_{l3} decays were used not only for the calibration of the track quality cuts described in the previous section but also for the efficiency calibration of all three-particle identification detectors, the gas Cherenkov counter, the electromagnetic shower counter and the muon identifier. Figure 20(a) shows the effective mass $(m_{\pi^+\pi^-})$ distribution of
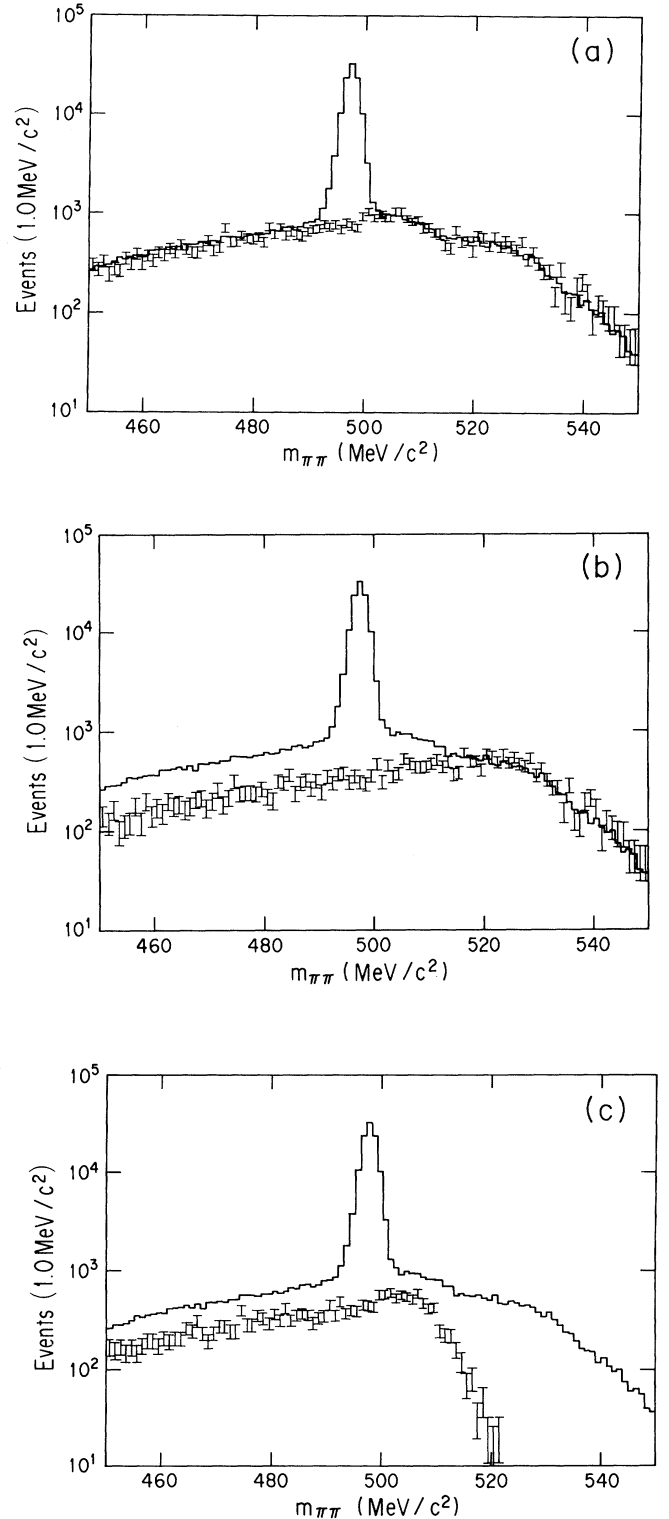

FIG. 20. (a) Effective mass $(m_{\pi^+\pi^-})$ distribution of the events collected by the $\pi^+\pi^-$ trigger assuming that both particles were pions for θ^2 less than 3×10^{-6} (rad)^2. I indicates the Monte Carlo results described in the text and the size of the bar indicates the statistical uncertainty; (b) the contribution from the $K_L^0 \to \pi e\nu$ decay; (c) from the $K_L^0 \to \pi\mu\nu$ decay both obtained by the Monte Carlo calculation.

the events collected by the $\pi^+\pi^-$ trigger with θ^2 less than 3×10^{-6} rad^2. The effective mass was calculated by assuming that both particles were pions. We see a clear peak due to the $K_L^0 \to \pi^+\pi^-$ decay with a flat background about 2 orders of magnitude smaller than the peak value. The background distribution was well reproduced by a Monte Carlo calculation as shown in the figure. The distributions of the Monte Carlo generated $K_L^0 \to \pi e \nu$ and $K_L^0 \to \pi \mu \nu$ events were normalized to the numbers of events in the two regions $470 < m_{\pi^+\pi^-} < 485$ MeV/c^2 and $510 < m_{\pi^+\pi^-} < 525$ MeV/c^2. Figures 20(b) and 20(c) show the contributions from the $K_L^0 \to \pi e \nu$ and $K_L^0 \to \pi \mu \nu$ decays, separately.

The π, e, and μ samples which were used for the efficiency calibration of the particle identification counters were obtained from the data as follows.

To select the pion from the $K_L^0 \to \pi e \nu$ decay in one of arms it was tagged by selecting an event in the mass regions $m_{\pi^+\pi^-} < 484$ MeV/c^2 and $m_{\pi^+\pi^-} > 511$ MeV/c^2 and by requiring an electron in the other arm. The absence of signals in the electron and muon identifiers except for the detector being calibrated was required in the pion arm. The electrons from the $K_L^0 \to ee\gamma$ decay was a possible source of background in this pion sample. However, its branching ratio is relatively small and vetoing an electron in the pion arm reduced this background to a negligible level. The pions which decayed in flight was also a source of contamination. The fraction of the pions which decayed before $W5$ but remained in the pion sample after the track quality and vertex cuts was estimated by a Monte Carlo calculation, and this was corrected for in the efficiency calculation. The number of pions used was $(4-6) \times 10^5$ in each arm.

To select the electron from the $K_L^0 \to \pi e \nu$ decay in one of arms it was tagged by requiring a pion in the other arm. For the calibration of the gas Cherenkov counter the electron sample was selected in the region $m_{\pi^+\pi^-} > 511$ MeV/c^2 where the K_{e3} decay dominated. The additional requirement was the presence of a shower counter signal and the absence of a muon identifier signal in the electron arm. The number of this electron sample in each arm was about 9×10^4. The fraction of the contamination of this sample by the other particles was estimated to be 1.2×10^{-4} from a combination of the misidentification factors of the counters used for this selection. For the calibration of the electromagnetic shower counter the electron sample was selected in the regions, $m_{\pi^+\pi^-} < 484$ MeV/c^2 and $m_{\pi^+\pi^-} > 511$ MeV/c^2, and the presence of a gas Cherenkov counter signal and the absence of a muon identifier signal were required in the electron arm. The number of this sample in each arm was about 1.7×10^5 and the fraction of the impurity in this sample was estimated to be 2.8×10^{-4}. For a check of the muon identifier response to electrons we used a good electron sample identified by both electron identifiers in the electron arm.

For muon selection the muon from the $K_L^0 \to \pi \mu \nu$ decay in one of the arms was tagged by requiring a pion in the other arm in the mass region below the $K_L^0 \to \pi^+\pi^-$ peak. The muon sample used for the calibration of one of the electron identifiers was well purified by requiring the presence of a signal in the muon identifier and the absence of a signal in the other electron identifier in the muon arm. However, the muon sample for the calibration of the muon identifier was not so pure as that used for the calibration of the other detectors. The muon sample for the muon identifier was selected and its purity was checked as follows. Pions were the dominant contaminant of this muon sample, because electrons were almost completely removed by requiring the absence of signals in both electron identifiers. In order to reduce the pion contamination from the $K_L^0 \to \pi^+\pi^-\gamma$ decay, the sample in the region $m_{\pi^+\pi^-} < 480$ MeV/c^2 was used. In the pion arm the pion momentum was required to be greater than 1.5 GeV/c, which is the momentum of a muon penetrating up to the third layer of the counter arrays of the muon identifier, and the absence of signals in the last three layers of the muon identifier was required to tighten the pion identification criteria. This tight pion requirement in the pion arm reduced the pion contamination in the muon arm due to the misidentification of the muon from the $K_L^0 \to \pi \mu \nu$ decay as a pion in the pion arm. In order to check the remaining pion contamination we imposed the above tight pion identification in both arms and calculated the number of $\pi^+\pi^-$ events (N_{obs}). The contribution of $\pi^+\pi^-$ events ($n_{\pi\pi}$) to the muon sample was estimated after correcting for the efficiency of the tight pion identification in the muon arm (η_π) as $n_{\pi\pi} = N_{\text{obs}}/\eta_\pi$. η_π was obtained by using a different pion sample taken from the K_{e3} region, and $n_{\pi\pi}$ was found to be only 0.52% of the muon sample. This 0.52% contamination came from two possible sources. One was the real $\pi^+\pi^-$ events from the tail of the $K_L^0 \to \pi^+\pi^-\gamma$ decay. It was estimated to be 0.28% by a Monte Carlo calculation, and the calibration value for the muon identifier efficiency was corrected for it. The remaining 0.24% was thought to come from the $K_{\mu3}$ decay whose muon in the pion arm was misidentified as a pion. We included this contribution in the error in the particle identification efficiencies. The number of muons in this sample was about 6×10^4 in each arm.

2. Electron identifiers

The gas Cherenkov counter and the electromagnetic shower counter were used for electron identification. The timing with respect to the trigger and the pulse height of the gas Cherenkov signal from the cell where the particle passed were examined. The timing with respect to the trigger was required to be between -2.5 and 3.0 nsec. The timing resolution was 0.60 nsec. Figure 21 shows the ADC distribution of the output pulses for electrons. The peak corresponds to five photoelectrons using the single-photoelectron value measured during a beam-off period. It was consistent with the fact that the pulse height distribution fits well the Poisson distribution with an average value of 5 as indicated in the figure. The threshold value for electrons was set at 300 which corresponded to 1.5 photoelectrons. Since the detection efficiency of the gas Cherenkov counter for electrons decreased at the boundaries of the four mirrors due to the
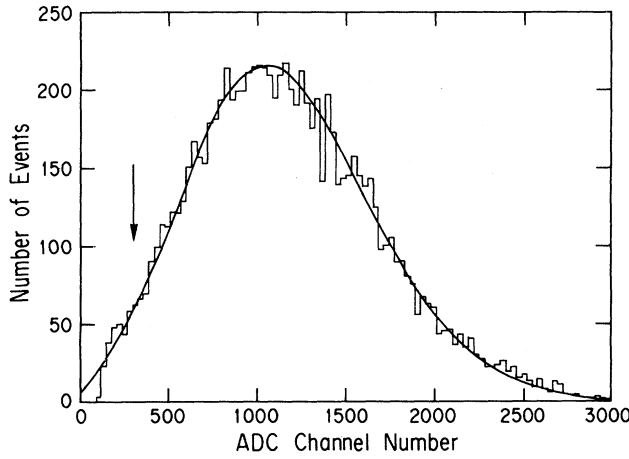
FIG. 21. ADC distribution of the output pulses of the gas Cherenkov counter for electrons. The solid curve shows a Poisson distribution with the mean value of 5.

distortions of the mirrors from the spherical shape, it was determined in each of 36 segmented areas in each arm. Figure 22 shows a lego plot of the gas Cherenkov counter efficiency $\epsilon_e^{Ch}(X, Y)$, where (X, Y) represents the hit point on the plane at the mirror position. The probabilities of misidentifying muons and pions as electrons, ϵ_μ^{Ch} and ϵ_π^{Ch}, were determined as averaged values for the pion and muon samples, respectively.

For the electromagnetic shower counter no timing requirement was applied. The energy deposit (E) was obtained by summing all signals from the counters within 12 cm for the forward section and 16 cm for the backward section on both sides of the track. The gains of all photomultipliers and the light attenuation lengths of all counters were determined by using the electron sample from the K_{e3} decay. The energy resolution for electrons was obtained to be $\sigma(E)/E = 0.20/\sqrt{E(\text{GeV})} + 0.022$ as shown in Fig 23. Using the EGS code [19], the energy res-
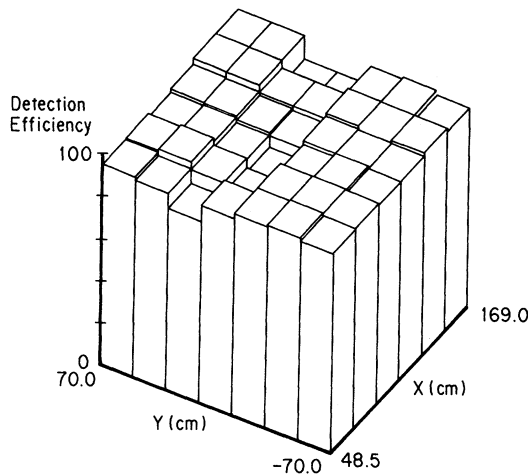

FIG. 22. Position dependence of the detection efficiency of the gas Cherenkov counter for electrons.
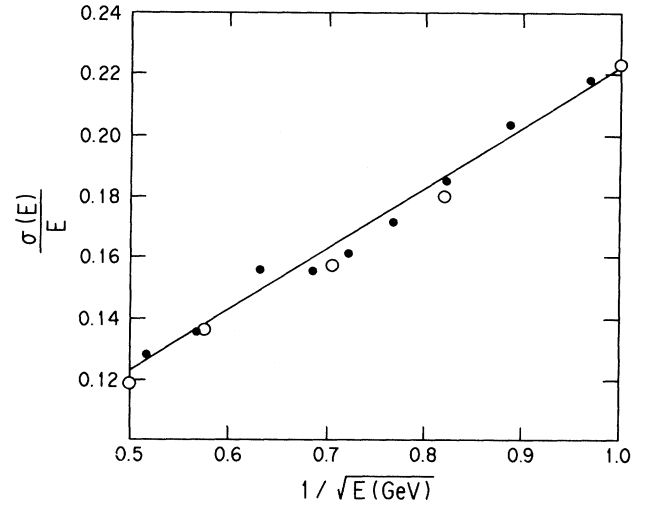

FIG. 23. Energy resolution of the electromagnetic shower counter for electrons for various electron energies. The solid and open circles show the results from real data and from an EGS calculation, respectively. For the EGS results an energy independent term of 0.022 were added. The solid line expresses $\sigma(E)/E = 0.20/\sqrt{E(\text{GeV})} + 0.022$.

olution was calculated from the fluctuation of the energy deposit in the layers of scintillator. The calculated result with the constant term of 0.022 well reproduced the experimental data as shown in the figure. The shower position was calculated by taking the weighted mean of the center positions of the hit counters using the energy deposit as the weight. The shower position was required to be within 5.5 cm on both sides of the track to be acceptable. Figure 24 shows E/P distributions for electrons, pions and muons where P is the momentum measured by the spectrometer. $E/P > 0.7$ was required to separate electrons from pions and muons. In addition, it was required that the energy deposit in the forward section, that in the backward section and the total energy deposit have to be greater than 139, 44, and 500 MeV, respectively. The detection efficiency of the electromagnetic shower counter for electrons, $\epsilon_e^{EM}(P)$, was determined at 18 momentum bins as shown in Fig. 25. The probabilities of misidentifying pions and muons as electrons, ϵ_π^{EM} and ϵ_μ^{EM}, were determined as averaged values of the samples used for the calibration.

3. Muon identifier

The timings of MU1 and MU2 signals and those of MU3 and MU4 signals were required to be within 2.5 and 3.0 nsec with respect to the trigger after correcting for the propagation time in the counter. The timing resolution for MU1, MU2, MU3, and MU4 was 0.78, 0.66, 0.80, and 0.91 nsec, respectively. A hit candidate in each layer was searched for around the track extrapolated from the spectrometer. For MU1 and MU2 the counters whose center positions were within ±33 cm of

the track were examined. For MU3 and MU4, an examination within a relatively large width of ± 42 cm was performed in order to compensate for multiple Coulomb scattering in iron. For muon identification the presence of a last hit in MU2, MU3, or MU4 was required. Figures
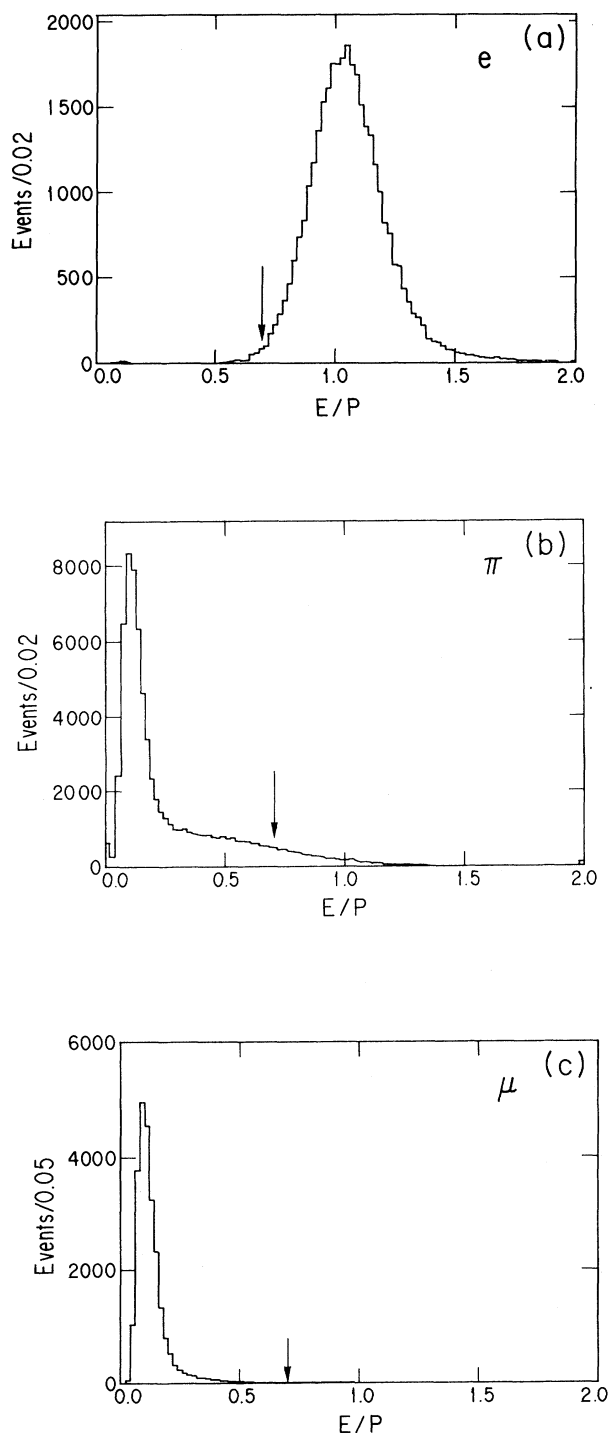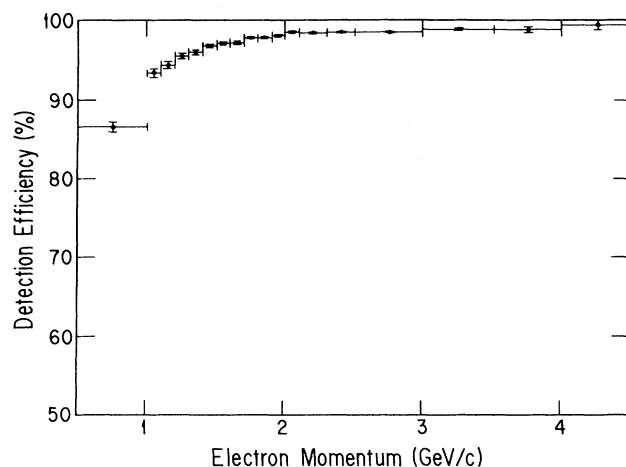
FIG. 25. Momentum dependence of the detection efficiency of the electromagnetic shower counter for electrons.

26(a)–26(c) show the momentum distributions of muons whose last hit was in MU2, MU3, and MU4, respectively. From these figures muons were required to have the momentum (P) range, $1.0< P < 1.7$ GeV/c if its last hit was in MU2, $1.3 < P < 2.6$ GeV/c if it was in MU3 and $P > 1.7$ GeV/c if it was in MU4. The minimum numbers of layers with hits along the track were required to be 2, 2, and 3 if the last hit was in MU2, MU3, and MU4, respectively. The detection efficiency of the muon identifier for muons and the probability of misidentifying pions as muons, $\epsilon_\mu^{MU}(P)$ and $\epsilon_\pi^{MU}(P)$, were determined in 17 momentum bins as shown in Figs. 27(a) and 27(b). The probability of misidentifying electrons as muons ϵ_e^{MU} was determined as an averaged value over the electron sample.

The obtained values of the detection efficiencies of all three-particle identification detectors in both arms for electrons, muons, and pions are shown in Table I, where ϵ_e^{Ch}, ϵ_e^{EM}, ϵ_μ^{MU}, and ϵ_π^{MU} were also given as averaged values over the samples used for the calibration.

4. Particle identification efficiencies for the two-body decay modes

Each track was identified as an electron, muon, or pion from the combination of signals in the particle identifiers, and then the decay mode of each event was identified by combining the information for both arms. The particle identification efficiency for each decay mode was the product of the efficiencies of the detectors. If they were momentum or position dependent, they were integrated over appropriate dependent variables. The particle identification efficiency for the $K_L^0 \to \mu e$ decay $[\epsilon(\text{PID})_{\mu e}]$ was given as

FIG. 24. Distributions of the E/P for (a) electrons, (b) pions, and (c) muons. The arrow at $E/P = 0.7$ is the cutoff value.

TABLE I. Average particle identification efficiencies of the samples from the K_{l3} decays. Refer to the text for the explanations of the labels.

Detector	Particle	Label	Efficiency (%) Left arm	Efficiency (%) Right arm
Cherenkov counter	e	ϵ_e^{Ch}	94.46± 0.27	91.27 ± 0.27
	μ	ϵ_μ^{Ch}	0.180±0.018	0.225 ±0.019
	π	ϵ_π^{Ch}	0.128±0.012	0.190 ±0.015
Shower counter	e	ϵ_e^{EM}	94.09± 0.29	94.40 ± 0.26
	μ	ϵ_μ^{EM}	1.673±0.054	1.642 ±0.052
	π	ϵ_π^{EM}	9.363±0.073	10.913±0.079
Muon identifier	e	ϵ_e^{MU}	0.242±0.013	0.257 ±0.013
	μ	ϵ_μ^{MU}	90.74± 0.27	90.08 ± 0.27
	π	ϵ_π^{MU}	1.94 ± 0.29	1.88 ± 0.29

$$\epsilon(\text{PID})_{\mu e} = \frac{1}{2}\left(\int \epsilon_{\mu L}^{MU}(P_L)(1 - \epsilon_{\mu L}^{EM})(1 - \epsilon_{\mu L}^{Ch})(1 - \epsilon_{eR}^{MU}) \right.$$

$$\left. \times \epsilon_{eR}^{EM}(P_R)\epsilon_{eR}^{Ch}(X_R,Y_R)\Omega_{\mu e}(P_L,P_R,X_R,Y_R)dP_L dP_R dX_R dY_R + L \leftrightarrow R \right) , \tag{6}$$

where suffices L and R refer to the left and right arms and $\Omega_{\mu e}$ is the density distribution of events for the $K_L^0 \to \mu e$ decay which was obtained by a Monte Carlo calculation.

For the $K_L^0 \to ee$, $K_L^0 \to \mu\mu$, and $K_L^0 \to \pi^+\pi^-$ decays the identification efficiencies, $\epsilon(\text{PID})_{ee}$, $\epsilon(\text{PID})_{\mu\mu}$, and $\epsilon(\text{PID})_{\pi\pi}$ were given as

$$\epsilon(\text{PID})_{ee} = \int (1 - \epsilon_{eL}^{MU})\epsilon_{eL}^{EM}(P_L)\epsilon_{eL}^{Ch}(X_L,Y_L)(1 - \epsilon_{eR}^{MU})\epsilon_{eR}^{EM}(P_R)$$

$$\times \epsilon_{eR}^{Ch}(X_R,Y_R)\Omega_{ee}(P_L,X_L,Y_L,P_R,X_R,Y_R)dP_L dX_L dY_L dP_R dX_R dY_R , \tag{7}$$

$$\epsilon(\text{PID})_{\mu\mu} = \int \epsilon_{\mu L}^{MU}(P_L)(1 - \epsilon_{\mu L}^{EM})(1 - \epsilon_{\mu L}^{Ch})\epsilon_{\mu R}^{MU}(P_R)(1 - \epsilon_{\mu R}^{EM})(1 - \epsilon_{\mu R}^{Ch})\Omega_{\mu\mu}(P_L,P_R)dP_L dP_R , \tag{8}$$

and

$$\epsilon(\text{PID})_{\pi\pi} = \int [1 - \epsilon_{\pi L}^{MU}(P_L)](1 - \epsilon_{\pi L}^{Ch})[1 - \epsilon_{\pi R}^{MU}(P_R)](1 - \epsilon_{\pi R}^{Ch})\Omega_{\pi\pi}(P_L,P_R)dP_L dP_R . \tag{9}$$

No information of the electromagnetic shower counter was used in pion identification. The values of $\epsilon(\text{PID})_{\mu e}$, $\epsilon(\text{PID})_{ee}$, $\epsilon(\text{PID})_{\mu\mu}$, and $\epsilon(\text{PID})_{\pi\pi}$ were 0.744 ± 0.005, 0.730 ± 0.004, 0.763 ± 0.006, and 0.937 ± 0.003, respectively. The errors were dominated by the statistical errors of the samples used for the calibration.

F. Monte Carlo simulation

In order to calculate the geometrical acceptances and to check the experimental data a Monte Carlo simulation program was developed. It was assumed that K_L^0's were produced uniformly in the production target and were isotropically emitted from it. They were required to pass through the collimators in the neutral beam line. The K_L^0 momentum was given by a spectrum which reproduced the measured K_L^0 momentum distribution obtained from the $K_L^0 \to \pi^+\pi^-$ events. The K_L^0 decayed with a mean life of 5.17 nsec [9] at the decay point isotropically in its

rest system and the decay products were transformed to the laboratory system. For the K_{l3} decays the standard parametrization of the V-A Dalitz plot density given in [9] was used. Each trajectory of secondary particles was tracked through the decay chamber and the spectrometer up to the second hodoscope $H2$. In the spectrometer region the particle trajectory was traced in 46 steps by the Runge-Kutta method [20], using the measured magnetic field. Multiple Coulomb scattering in the decay chamber, vacuum windows, drift chambers, helium bags, hodoscopes, gas Cherenkov counter, and small gaps of air was included in the calculation at every step. The standard multiple Coulomb scattering formula [9] was used as the main Gaussian distribution. For the non-Gaussian tail the distribution numerically given by Marion and Zimmerman [21] was used to simulate large angle scattering. For the pion and muon decays the mean lives of 26.0 and 2197 nsec [9] were used. For the pion the $\pi \to \mu\nu$ decay was assumed, and the secondary muon trajectory was traced. For the muon the trajectory tracing pro-

cess was stopped where it decayed without further tracing the decayed products. The trajectory was required to path through the effective areas of all chambers and to satisfy the parallel or semiparallel requirement at the hodoscopes in each arm.

The hit wire number and drift length were calculated for each chamber. The drift length was smeared by a Gaussian distribution with the spatial resolution of the

chamber and was converted to the drift time using the space-time relation described in Sec. II B 2. The drift time was then converted to the channel number of TDC. The calibration parameters for the drift chambers, such as the space-time relation for each wire, the position of each chamber, the signal propagation time in the wire and dead-wire information were used in the simulation.

The x position of the track at the hodoscope was transformed to the hit counter number of the hodoscope. The relative timing between the signals from the top and bottom photomultipliers was calculated using the y position of the track and the propagation time of light in the scintillator, and the TDC channel number was calculated after smearing the timing by a Gaussian distribution with the standard deviation equal to the time resolution.

To simulate the experimental conditions real data taken by random triggers generated by a pulse generator, which were regularly collected under various beam
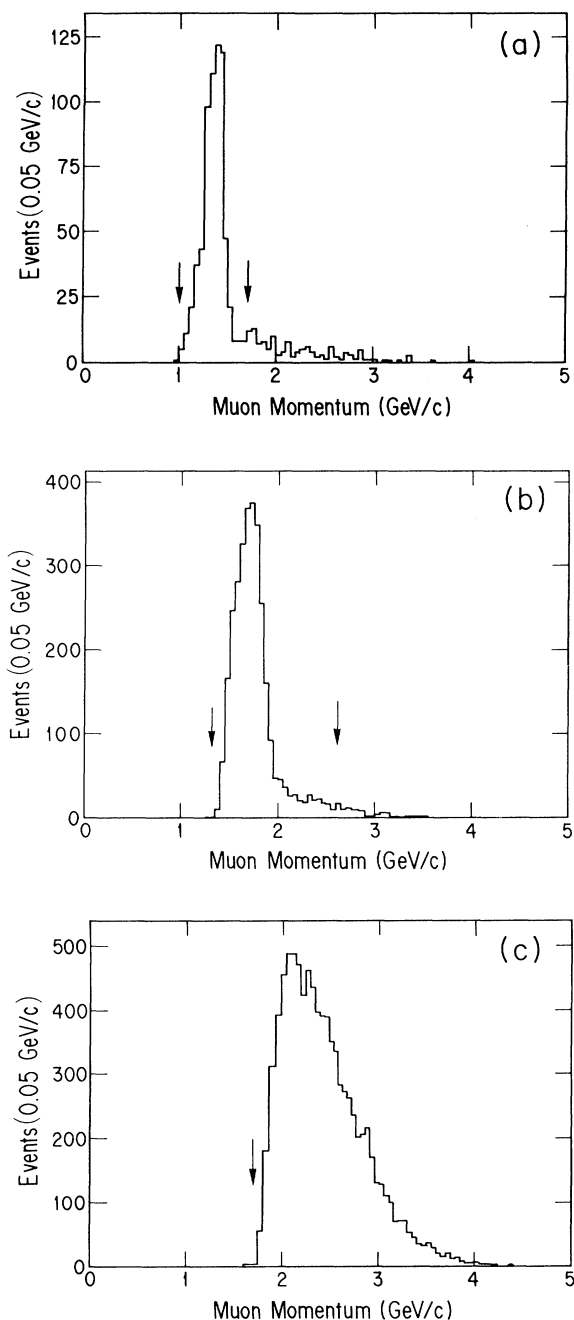
FIG. 26. Momentum distributions of muons whose last hit was in (a) $M2$, (b) $M3$, and (c) $M4$. The arrows indicate the muon selection criteria.
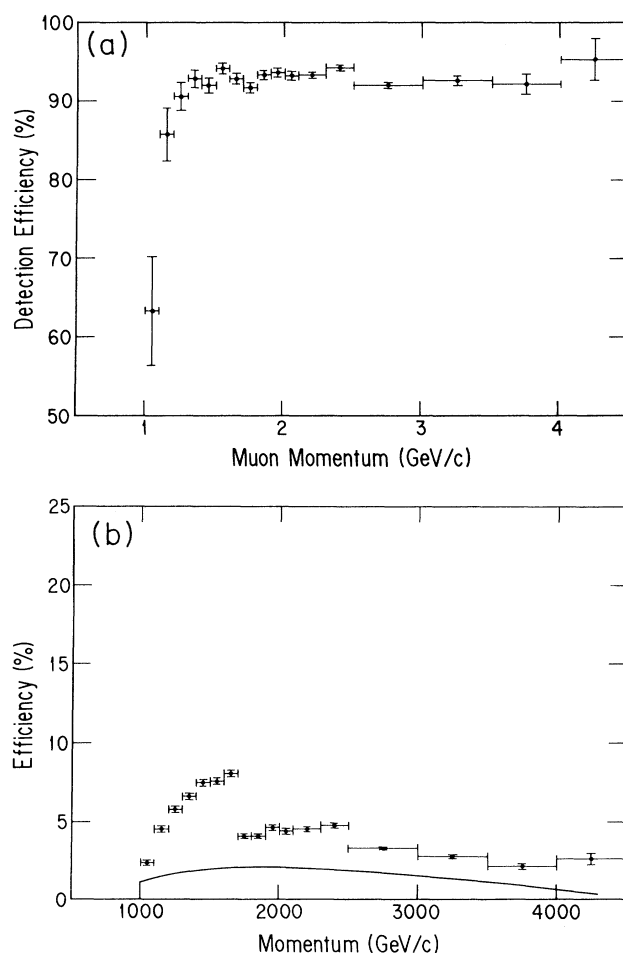

FIG. 27. Momentum dependences of (a) the detection efficiency of the muon identifier for muons and (b) its probability of misidentifying pions as muons, where it includes the muon contribution from the $\pi \to \mu\nu$ decay in flight. The solid curve in (b) shows the result of a Monte Carlo calculation of the muon contribution from the pion decay before $W5$ which was subtracted from the measured value in (b) to obtain the probability of misidentifying pions as muons, ϵ_π^{MU}.

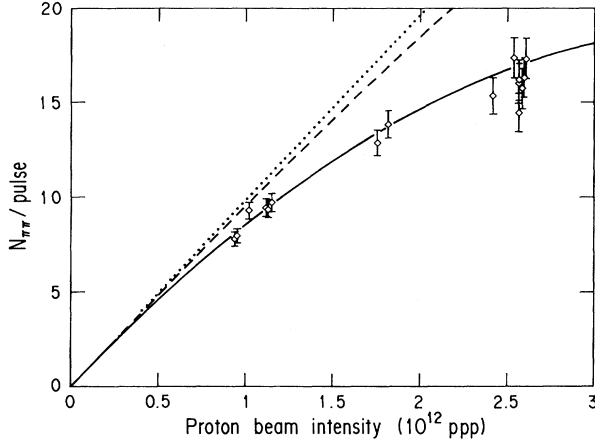FIG. 28. Beam intensity dependence of the yield of $K_L^0 \to \pi^+\pi^-$ events $(N_{\pi\pi})$ per beam pulse. The solid line represents the results from a calculation with accidental hits in the drift chambers and the hodoscopes of randomly triggered events at various beam intensities superposed on Monte Carlo events. The dotted and dashed lines represent those from the calculations without this superposition and with superposition only on the hodoscope hits, respectively.

conditions, were superposed onto the Monte Carlo data. The superposition was made for the drift chamber and hodoscope data. When the same wire or counter had both real and accidental signals, the earlier signal in timing was taken. Monte Carlo events were reconstructed by the same tracking programs used for the actual events, and were checked by the same selection criteria. Figure 28 shows the number of $K_L^0 \to \pi^+\pi^-$ events per beam pulse for various primary beam intensities. The yields were not proportional to the primary beam intensity due to the fact that the tracking efficiency depended on the counting rates of the detectors, but they were well reproduced by the Monte Carlo calculations including those for which randomly triggered data collected at the corresponding primary beam intensity were superposed.

IV. EXPERIMENTAL RESULTS

A. Sensitivities for the branching ratios

A single-event sensitivity for each $K_L^0 \to ll'$ (l, l' represent charged leptons) decay, $X_{\mathrm{SES}}(K_L^0 \to ll')$ was obtained by using the number of the $K_L^0 \to \pi^+\pi^-$ events as the normalization factor:

$$X_{\mathrm{SES}}(K_L^0 \to ll') = \frac{1}{N_{\pi^+\pi^-}} \frac{A_{\pi^+\pi^-}}{A_{ll'}} \frac{\epsilon(\mathrm{PID})_{\pi^+\pi^-}}{\epsilon(\mathrm{PID})_{ll'}}$$
$$\times C(\mathrm{DAQ})\epsilon(\mathrm{NI})_{\pi^+\pi^-}$$
$$\times B(K_L^0 \to \pi^+\pi^-) , \qquad (10)$$

where $B(K_L^0 \to \pi^+\pi^-)$ is the branching ratio of the $K_L^0 \to \pi^+\pi^-$ decay, $(2.03 \pm 0.04) \times 10^{-3}$ [9]. $N_{\pi^+\pi^-}$ is the number of the observed $K_L^0 \to \pi^+\pi^-$ events after

correcting for the prescaling factor. $A_{ll'}$ and $\epsilon(\mathrm{PID})_{ll'}$ represent the acceptance and the particle identification efficiency, and $A_{\pi^+\pi^-}$ and $\epsilon(\mathrm{PID})_{\pi^+\pi^-}$ represent those for the $K_L^0 \to \pi^+\pi^-$ decay. $C(\mathrm{DAQ})$ and $\epsilon(\mathrm{NI})_{\pi^+\pi^-}$ are the correction factors for the effects of the dead time during data taking and of the loss of pions by nuclear interactions.

It is worth mentioning that the acceptance for each leptonic decay contributes as a ratio with respect to the $K_L^0 \to \pi^+\pi^-$ acceptance and that the corrections for the acceptances and the particle identification efficiencies follow up changes in the running condition, because they were calibrated by using the data simultaneously collected in the experiment.

1. Number of $K_L^0 \to \pi^+\pi^-$ events

Figure 29 shows a plot of the effective mass $(M_{\pi^+\pi^-})$ vs the collinearity angle squared (θ^2) for a representative sample of 1000 $\pi^+\pi^-$ events. Most of the events are clustered around the point $M_{\pi^+\pi^-} = M_{K_L^0}$ and $\theta^2 = 0$, which corresponds to the $K_L^0 \to \pi^+\pi^-$ decay. Figures 30(a) and 30(b) are the $M_{\pi^+\pi^-}$ distribution for all $\pi^+\pi^-$ events for $\theta^2 < 3$ mrad^2 and the θ^2 distribution for $493 < M_{\pi^+\pi^-} < 502$ MeV/c^2, respectively. The distributions were well reproduced by a Monte Carlo calculation which simulated the $K_L^0 \to \pi^+\pi^-$ decay. The resolutions for $M_{\pi^+\pi^-}$ and θ^2 were 1.28 MeV/c^2 and 0.92 mrad^2, respectively. The fiducial region for the $K_L^0 \to \pi^+\pi^-$ decay as well as for the $K_L^0 \to ll'$ decays was defined as the region bounded by $493 < M_{\pi^+\pi^-} - (M_{ll'}) < 502$ MeV/c^2 and $\theta^2 < 3$ mrad^2. The acceptable $M_{\pi^+\pi^-}$ and θ^2 ranges were more than three times their resolutions. A slight shift of the $M_{\pi^+\pi^-}$ peak and the small tail in the low mass region were observed. Some contribution to the tail was expected from the $K_L^0 \to \pi^+\pi^-\gamma$ decay [22,23] as shown in Fig. 31. In order to find a reason for the shift we tried to extend the fringe field of the first spectrometer magnet into the decay volume. The field strength of about 1 G m was enough to cause the same amount of shift of
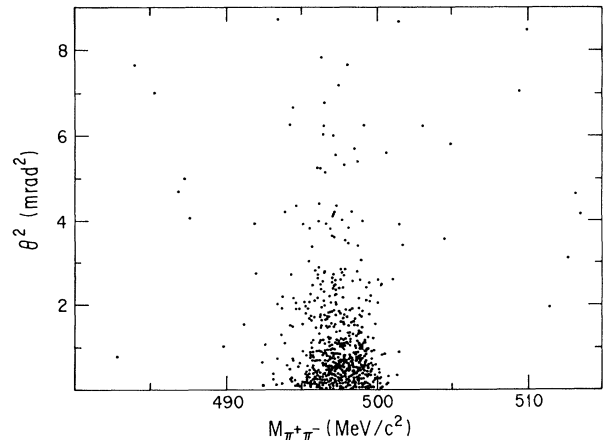

FIG. 29. Scatter plot of $M_{\pi^+\pi^-}$ vs θ^2 for representative 10^3 $\pi^+\pi^-$ events.
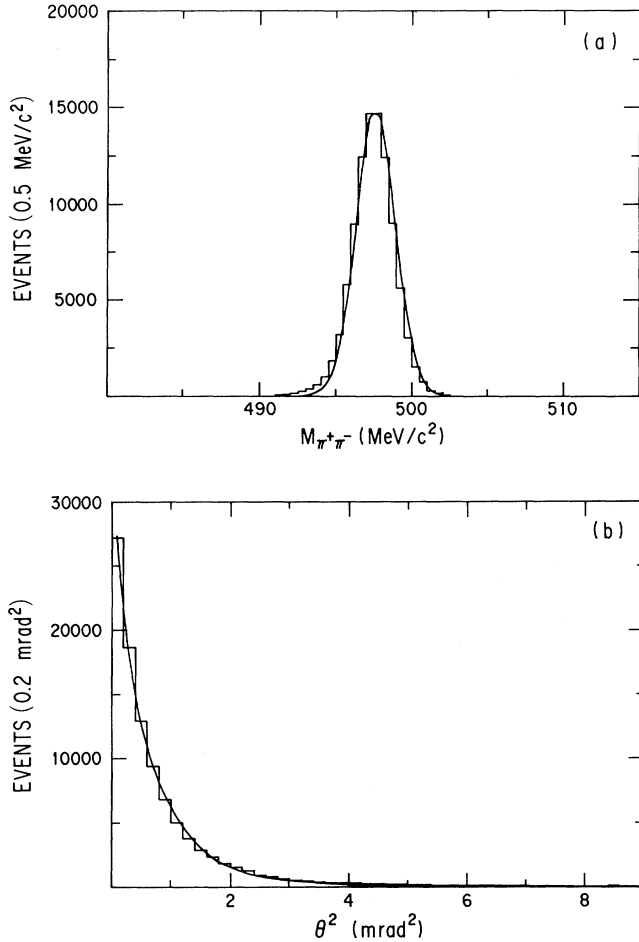
FIG. 30. Distributions of (a) $M_{\pi^+\pi^-}$ with $\theta^2 < 3$ (mrad)^2 and (b) θ^2 with $493< M_{\pi^+\pi^-} < 502$ MeV/c^2 for all the $\pi^+\pi^-$ events. The solid lines are the distributions of the Monte Carlo $K_L^0 \to \pi^+\pi^-$ events normalized to contain the same number of events in the fiducial region.

the peak position. However, no adjustment was made for the shift, since the shift was too small to change the acceptances.

The number of $\pi^+\pi^-$ events in the fiducial region was 1.588×10^5. The number of background events was estimated to be 1.5×10^3 by averaging the numbers of events in the 9 MeV/c^2 wide regions adjacent to the mass fiducial boundaries: $484< M_{\pi^+\pi^-} < 493$ MeV/c^2 and $502< M_{\pi^+\pi^-} < 511$ MeV/c^2 with $\theta^2 < 3$ mrad^2. The number of $K_L^0 \to \pi^+\pi^-$ events was determined to be 1.573×10^5 by subtracting the background events from the events in the fiducial region. It was corrected for the prescaling factor of the $\pi^+\pi^-$ trigger, and $N_{\pi^+\pi^-}$ was determined to be $(6.374\pm0.017\pm0.060)\times10^7$. The first uncertainty was the statistical fluctuation (0.26%) and the second one is the systematic uncertainty due to the background subtraction (0.94%). The number of background events itself was used as the systematic uncertainty due to the subtraction.
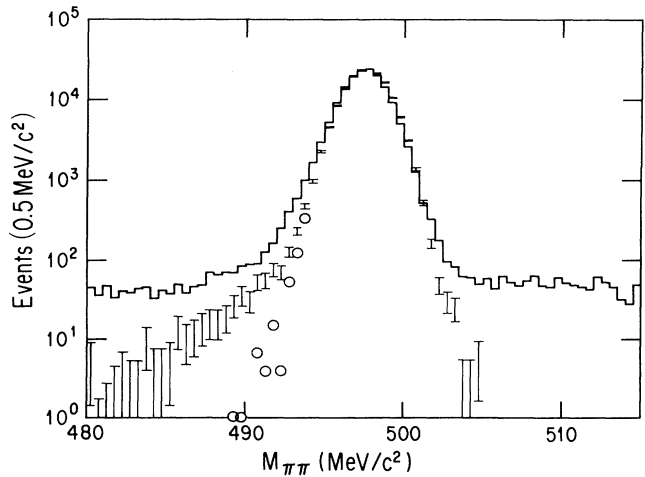

FIG. 31. Semilog plot of the distribution of $M_{\pi^+\pi^-}$ with $\theta^2 < 3$ (mrad)^2 for all the $\pi^+\pi^-$ events. The distribution with the error bars shows the result of a Monte Carlo calculation for both $K_L^0 \to \pi^+\pi^-$ and $K_L^0 \to \pi^+\pi^-\gamma$ decays. The circles in the lower mass region represent the contribution only from the $K_L^0 \to \pi^+\pi^-$ decay.

As a check of $N_{\pi^+\pi^-}$ the number of $K_L^0 \to \pi^+\pi^-$ events was also calculated from the $\pi^+\pi^-$ mass distribution without requiring particle identification. The distribution was previously shown in Fig. 20(a). The background distribution was calculated by a Monte Carlo calculation, where the contributions from both K_{e3} and $K_{\mu3}$ decays were normalized to the yields in the regions $470 < M_{\pi^+\pi^-} < 485$ MeV/c^2 and $510 < M_{\pi^+\pi^-} < 525$ MeV/c^2, as described previously. The number of $K_L^0 \to \pi^+\pi^-$ events without particle identification, $N_{\pi^+\pi^-}^{\mathrm{NID}}$, was obtained from the number of events in the fiducial region (1.809×10^5) after subtracting the background of 1.20×10^4 events. Using the prescaling factor and the pion identification efficiency of 0.937, $N_{\pi^+\pi^-}^{\mathrm{NID}}$ was found to be 6.41×10^7, which agreed with $N_{\pi^+\pi^-}$ within the systematic uncertainty.

The K_S^0 contamination due to neutron interactions and the regeneration by the residual gas in the decay chamber were estimated to be less than 10^{-5} and 10^{-8} of $N_{\pi^+\pi^-}$, respectively. Figure 32 shows the proper time distribution of the $K_L^0 \to \pi^+\pi^-$ events. It was well reproduced by a Monte Carlo calculation assuming the K_L^0 mean life of 51.7 nsec.

2. Acceptance

The acceptance comprised the geometrical acceptance, the track reconstruction efficiency including the effect of the track quality cuts, the correction for the fiducial and event cuts.

The geometrical acceptance for each two-body decay was calculated by a Monte Carlo calculation. Since all four decays were similar in the decay kinematics, most of the effects such as those due to the position cuts to define
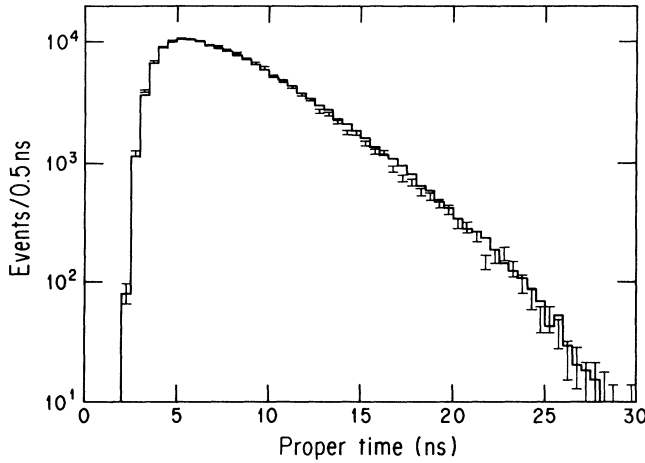
FIG. 32. Distribution of the proper time of the parent particle for all $\pi^+\pi^-$ events. The distribution with error bars shows the results of a Monte Carlo calculation with the K_L^0 mean life of 51.7 nsec.

the track acceptance were common to all decay modes and were nearly equal, and by taking the ratio of the geometrical acceptance for each leptonic decay to that for the $K_L^0 \to \pi^+\pi^-$ decay ($A_{\pi^+\pi^-}/A_{ll'}$) they canceled out. However, since there were slight differences among the decay modes in the distributions of particle momentum, etc., the localized detector inefficiencies had slightly different effects on the acceptances. Actually these differences were very small. For example, the effect of the dead wires, the number of which was at most 10 out of 4864 wires, was taken into consideration in the calculation, but its effect on the relative acceptances was negligibly small. The decreased efficiency of the drift chambers and the hodoscopes in localized regions due to accidental hits were also included in the calculation by superposing the randomly triggered data, but it was found to affect little the relative acceptances from a comparison between the calculations with and without the superposition. These corrections to the relative acceptances amounted to about 1% altogether.

The tracking efficiency was checked by analyzing Monte Carlo events with the superposition of the data collected under various beam conditions by the same tracking method. Although the tracking efficiency for each decay depended on the beam condition, the ratio was stable against it. The effect of the track χ^2 cut was negligibly small and the Δ_{UD} was investigated by taking the double ratio $(\eta_{\mu,e}/\eta_\pi)_{\text{data}}/(\eta_{\mu,e}/\eta_\pi)_{\text{MC}}$ by using the track samples from the K_{l3} decays as described previously.

The percentages of events which fell in the fiducial region among the reconstructed events were obtained from a Monte Carlo calculation to be 94.7±01, 97.8 ± 0.1, 97.0 ± 0.1, and 98.2 ± 0.1 % for the $K_L^0 \to \pi^+\pi^-$, μe, ee, and $\mu\mu$ decays, respectively. The larger correction for the $K_L^0 \to \pi^+\pi^-$ decay was due to the relatively large effect of the pion decay in flight. The differences in the fiducial region acceptance among the leptonic decays were very

small: at most 1.2%.

The corrections and their errors for the event cuts described in Sec. III D were very small, because these cuts were quite loose and passed more than 99% of the genuine events. The requirement for the muon momentum to be greater than 1 GeV/c reduced the acceptance for the $K_L^0 \to \mu e$ and $\mu\mu$ decays by 7.2 and 11 %, respectively. The values of the acceptance ratios thus obtained and used for the calculation of the single-event sensitivities were $A_{\pi^+\pi^-}/A_{\mu e} = 1.072 \pm 0.011$; $A_{\pi^+\pi^-}/A_{ee} = 1.067 \pm 0.011$; and $A_{\pi^+\pi^-}/A_{\mu\mu} = 1.191 \pm 0.013$.

3. Correction for dead-times difference

The dead time occurred due to the inhibition of a trigger during the busy time of the data-taking system to process the data initiated by the trigger just prior to it. The dead time occurred typically 5% of the data taking time and it was essentially common to all triggers. However, the dead-time correction for the $K_L^0 \to \pi^+\pi^-$ decay was slightly different from those for the other decays because of the prescaling of the trigger. The $\pi^+\pi^-$ trigger after prescaling had a periodic time structure. If the inhibition was applied after prescaling, the $\pi^+\pi^-$ trigger was seldom inhibited by the previous $\pi^+\pi^-$ trigger. During the first three-quarters of the running time inhibition was applied after prescaling, and the dead time for the $\pi^+\pi^-$ trigger was a little shorter than those for the other triggers. The correction for these different dead times was estimated by using the average dead time and the ratio of the $\pi^+\pi^-$ trigger rate to the sum of the other trigger rates. In the last quarter of the running period inhibition occurred before prescaling and the dead time was the same for all triggers. The correction for the different dead times for the whole sample, $C(\text{DAQ})$, was 1.013 ± 0.003.

4. Pion loss by nuclear interactions

Since the pion interaction cross section was large in the energy range of the present experiment, the correction for pion nuclear interactions was an important correction. The interaction effect was separately investigated in two regions: the up- and downstream regions of $W5$.

If interaction occurred in the upstream region of $W5$, most of the tracks which underwent nuclear interactions were removed by the track quality cuts. Since there was very little material in it, the fractional loss of pions by nuclear interactions was very small and we estimated it to be $(6.6 \pm 1.3) \times 10^{-3}$ using the total cross section. The uncertainty originated from the ambiguities in the effective thickness of the material and the variation in the cross section.

In the downstream region from $W5$ to $H2$, the thickness of the material amounted to 9.7×10^{-2} nuclear collision lengths. The main material was the 1.5-cm-thick aluminum frame to support the mirrors of the gas Cherenkov counter. Not all the tracks which had nuclear interactions in this region were removed by the trigger

and the track analysis. The loss depended on the z position of the material with respect to the positions of $H1$ and $H2$, the pion momentum and the elastic and inelastic differential cross sections. The loss was not small and could not be easily estimated by a simple calculation. Therefore, a special run in which we used the pions from the K_{e3} decay was performed. In one arm an electron was required so as to select the K_{e3} decay a pion was tagged in the other arm. In the pion arm only an $H1$ hit was required at the trigger stage. In the off-line analysis the reconstructed events without an $H2$ signal along the track in the pion arm were counted to estimate the loss due to nuclear interactions. Figure 33 shows the momentum dependence of the loss of pions by nuclear interactions obtained by this measurement. The open circles represent the result of a calculation using FLUKA [24], which is a Monte Carlo program developed at CERN for the nuclear cascade process. The detection efficiency of the $H2$ counter was calibrated by using an electron sample in the minimum bias run, where the hodoscope coincidence was not required in the trigger. It was $99.5 \pm 0.3\,\%$ after correcting for the electromagnetic interaction in the material before $H2$.

The overall correction for the pion loss by nuclear interactions for the $K_L^0 \to \pi^+\pi^-$ decay, $\epsilon(\mathrm{NI})$, was obtained by integrating the momentum-dependent loss over the pion momentum spectrum in both arms, and it was 0.937 ± 0.006. The error included the statistical error of the calibration sample and the systematic error which was estimated from the ambiguities in the determination of the geometrical edges of each $H2$ counter.

The corrections and their uncertainties described above are tabulated in Table II. Using these values the single event sensitivities for the $K_L^0 \to \mu e$, ee, and $\mu\mu$ decays were calculated to be $(4.08 \pm 0.11) \times 10^{-11}$, $(4.14 \pm 0.11) \times 10^{-11}$, and $(4.42 \pm 0.12) \times 10^{-11}$, respectively. The error in each single-event sensitivity was calculated by adding all uncertainties in quadrature.

B. $K_L^0 \to \mu e$

Figure 34 shows a scatter plot of $M_{\mu e}$ vs θ^2 for the μe events. The fiducial region is indicated by the solid lines. No event is seen in the fiducial region.

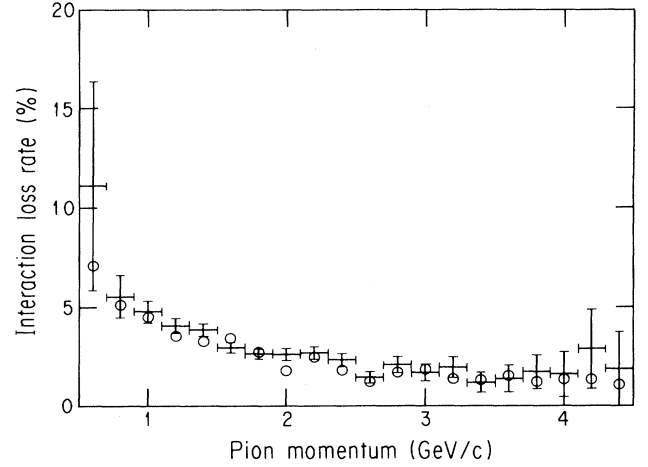In order to study the background a scatter plot of $M_{\mu e}$

FIG. 33. Momentum dependence of the nuclear interaction loss due to the material in the region between $H1$ and $H2$. The distribution with the error bars is the experimental data and the open circles indicate the result of the FLUKA simulation.

vs P_t is shown in Fig. 35, where P_t is the transverse momentum of the μe system with respect to the target-to-vertex direction. Figure 36(a) shows a histogram of $M_{\mu e}$ with $P_t < 20$ MeV/c. In the figure the results of a Monte Carlo calculation are superposed. The crosses indicate the contribution from the $K_L^0 \to \pi e \nu$ decay whose pion was misidentified as a muon. This is a dominant source of the background in the lower effective mass region, but it rapidly decreases near the kinematical limit of 483.4 MeV/c^2. The open circles indicate the contribution from the $\pi \to \mu \nu$ decay of the pion from the $K_L^0 \to \pi e \nu$ decay in the decay chamber. This contribution extends to the higher mass region, because the $\pi \to \mu \nu$ decay in the forward direction boosts the momentum of the muon beyond that of the parent pion. The sum of these two contributions is shown by the solid circles with error bars. These Monte Carlo events were normalized to the number of $K_L^0 \to \pi^+\pi^-$ events. The background in the mass region below the fiducial region is well explained by this sum.

However, there was an excess of events in the high mass region as seen by comparing Fig. 36(b) with Fig.

TABLE II. Numerical factors used for the calculation of the sensitivities.

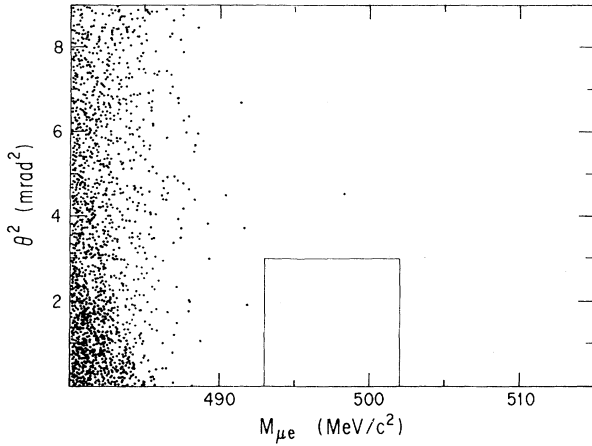| Factor	$K_L^0 \to \mu e$	Value $K_L^0 \to ee$	$K_L^0 \to \mu\mu$
$N_{\pi^+\pi^-}$		$(6.374 \pm 0.062) \times 10^7$	
$A_{\pi^+\pi^-}/A_{ll'}$	1.072 ± 0.011	1.067 ± 0.011	1.191 ± 0.013
$\epsilon(\mathrm{PID})_{\pi^+\pi^-}$		0.937 ± 0.003	
$\epsilon(\mathrm{PID})_{ll'}$	0.744 ± 0.005	0.730 ± 0.004	0.763 ± 0.006
$C(\mathrm{DAQ})$		1.013 ± 0.003	
$\epsilon(\mathrm{NI})_{\pi^+\pi^-}$		0.937 ± 0.006	
$B(K_L^0 \to \pi^+\pi^-)$		$(2.03 \pm 0.04) \times 10^{-3}$	
$10^{11} X_{\mathrm{SES}}(K_L^0 \to ll')$	$(4.08 \pm 0.11) \times 10^{-11}$	$(4.14 \pm 0.11) \times 10^{-11}$	$(4.42 \pm 0.12) \times 10^{-11}$

FIG. 34. Scatter plot of $M_{\mu e}$ vs θ^2 for the μe events. The box indicates the boundary of the fiducial region.

35. In the region $M_{\mu e} > 490$ MeV/c^2 and $P_t < 25$ MeV/c the number of experimental events is 36 and that of the calculation is 8. One of the sources for these high mass events could be due to double misidentification of both charged particles in the $K_L^0 \to \pi e \nu$ decay: the pion as an electron and the electron as a muon. This background was strongly suppressed due to the small probability of such particle misidentification. The number of background events due to double misidentification expected in the fiducial region in our experimental sensitivity was 5.2×10^{-5}. The other source was the $\pi \to \mu \nu$ decay in the spectrometer which was followed by a mismeasurement of the track momentum due to accidental hits in the drift chambers. This background was more highly suppressed by the track quality cuts than that due to the $\pi \to \mu \nu$ decay in the decay chamber. However, it can produce events with high μe effective mass. Figures 37(a) and 37(b) are scatter plots of $M_{\mu e}$ vs P_t and $M_{\mu e}$ vs θ^2, respectively. They show the result of a Monte Carlo calculation which simulated the $\pi \to \mu \nu$ decay in
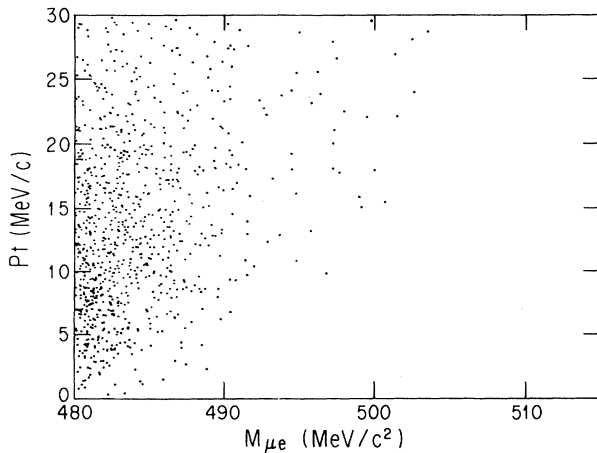
the spectrometer with accidental hits in the drift chambers and hodoscopes. The sensitivity of the calculation is 3.2 times higher than that of the experiment. The calculated events in Fig. 37(a) well reproduce the experimental events around the fiducial region as shown in Fig. 35. The number of events expected in the region $M_{\mu e} > 490$ MeV/c^2 and $P_t < 25$ MeV/c with our experimental sensitivity is 24 including the 8 events from the $\pi \to \mu \nu$ decay in the decay chamber. It is consistent with the experimental number of 36 within their statistical fluctuations. The number of background events expected in the fiducial region from the $\pi \to \mu \nu$ decay in the decay chamber was less than 0.1 and that from the pion decay in flight in the spectrometer region was zero even with the 3.2 times the experimental sensitivity as shown in Fig. 37(a).
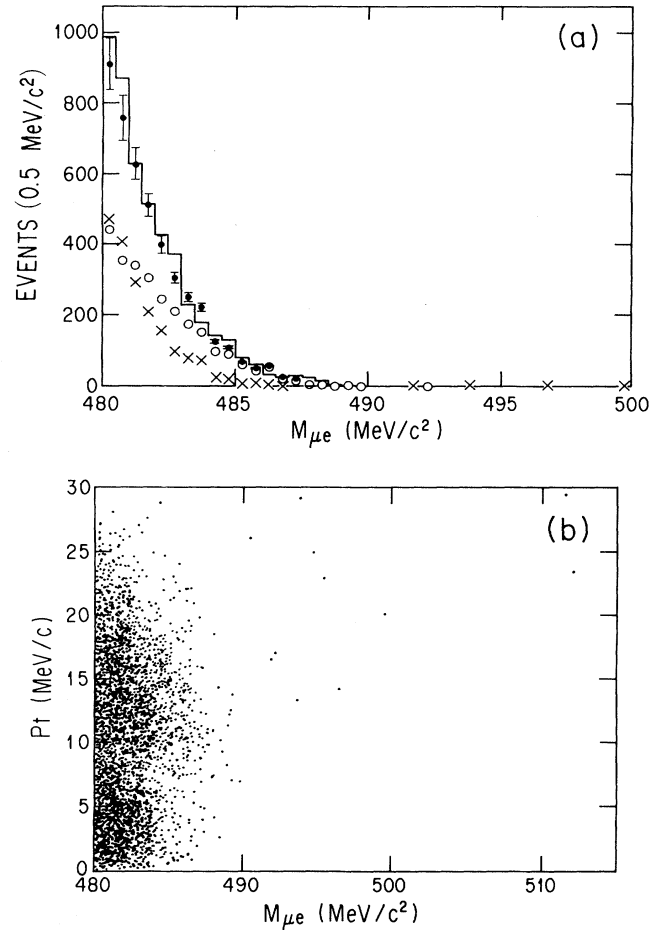

FIG. 36. (a) Distribution of $M_{\mu e}$ with $P_t < 20$ MeV/c for the μe events. The histogram and the distribution with the error bars are the results from the data and from the Monte Carlo generated $K_L^0 \to \pi e \nu$ events, respectively. Two components of the Monte Carlo generated events are also shown: the pion misidentification by the muon identifier by $\times$ and the pion decaying to a muon in the decay chamber by $\circ$. (b) Scatter plot of $M_{\mu e}$ vs P_t for the same Monte Carlo generated $K_L^0 \to \pi e \nu$ events as those used in (a).

FIG. 35. Scatter plot of $M_{\mu e}$ vs P_t for the μe events.

The high mass boundary of the real events in Fig. 35 increased with P_t, and this trend is also seen in the Monte Carlo plots in Figs. 36(b) and 37(b). This is qualitatively consistent with the above estimation that the dominant source of the background is the mismeasurement of the track momentum, which generally increases the effective mass with the resultant increase in P_t. This feature is quite different from the background from the double misidentification shown in Fig. 38.

Since no event is seen in the fiducial region not only in the experimental data but also in the calculation which explained the background well, we set an upper limit on the branching ratios at 90% confidence level as $B(K_L^0 \rightarrow \mu e) < 9.4 \times 10^{-11}$, using the single-event sensitivity given in the previous section. The error in the estimation of the sensitivity which affects the upper limit [25] was negligibly small.

C. $K_L^0 \rightarrow ee$

Figure 39 shows a scatter plot of $M_{e^+e^-}$ vs θ^2 for the e^+e^- events. There is one event in the fiducial region. A

FIG. 38. Scatter plot of $M_{\mu e}$ vs P_t for the Monte Carlo generated $K_L^0 \rightarrow \pi e \nu$ events with double misidentification $\pi \rightarrow e$ and $e \rightarrow \mu$. The sensitivity of the calculation corresponds to 3.3×10^5 times that of the experiment.

few events in the mass region below the fiducial region suggested that the one event might be in the tail of the structure in the low $M_{e^+e^-}$ region. Therefore, a plot of M_{ee} vs P_t in an extended mass region as shown in Fig. 40 was checked. No kinematical cut was applied to select the high mass events in the early stage of the track analysis for the e^+e^- events. This procedure was different from those for the other decay modes.

In the extended plot there were two structures: many events thickly clustered in the region of the effective mass below 470 MeV/c^2 and a considerable number of events were scattered in the region between 470 MeV/c^2 and the K_L^0 mass. There was no event above the K_L^0 mass. The high $M_{e^+e^-}$ boundaries of both structures decreased with P_t. This feature indicated that these events came from the K_L^0 decays associated with missing particles of light mass. In this case the larger the missing energy be-

FIG. 37. Scatter plots of (a) $M_{\mu e}$ vs θ^2 and (b) $M_{\mu e}$ vs P_t for the Monte Carlo generated $K_L^0 \rightarrow \pi e \nu$ events with the pion decaying to a muon in the spectrometer. The sensitivity of the calculation corresponds to 3.2 times that of the experiment.
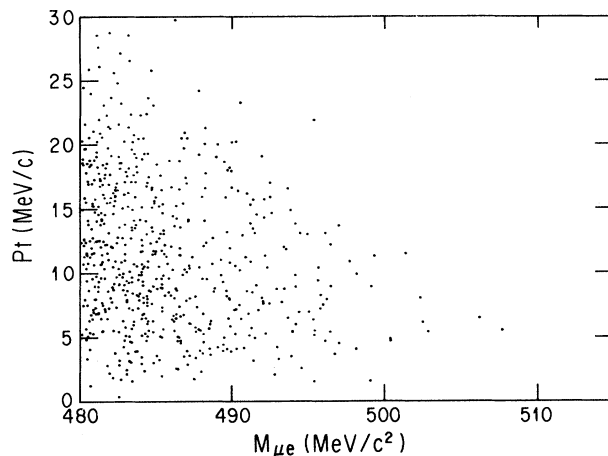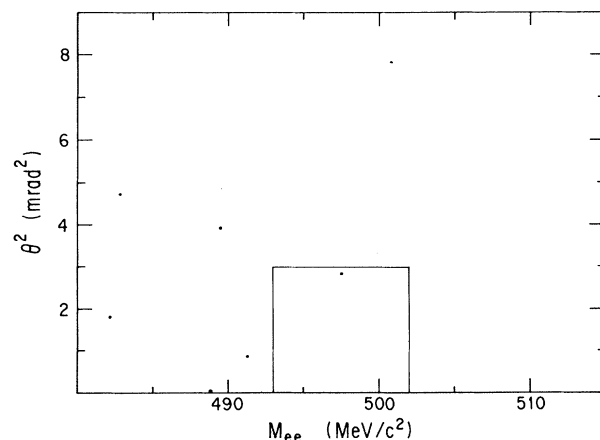

FIG. 39. Scatter plot $M_{e^+e^-}$ vs θ^2 for the e^+e^- events. The box indicates the boundary of the fiducial region.
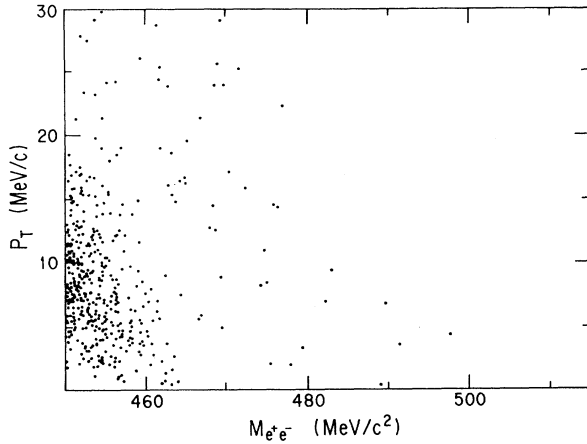
FIG. 40. Scatter plot of $M_{e^+e^-}$ vs P_t for the e^+e^- events in an extended mass region.

comes, the larger is the missing P_t. The source of the low mass cluster was the $K_L^0 \to \pi e \nu$ decay whose pion was misidentified as an electron. The high mass edge which was around $P_t = 0$ and $M_{e^+e^-} = 470$ MeV/c^2 was equal to the end point of the e^+e^- mass in which the pion from the $K_L^0 \to \pi e \nu$ decay was misidentified as an electron. The $K_L^0 \to ee\gamma$ decay with a missing gamma is a possible source of events above 470 MeV/c^2. Figure 41 shows the e^+e^- mass distribution for events with $P_t < 20$ MeV/c together with the results of a Monte Carlo calculation for the $K_L^0 \to \pi e \nu$ and $K_L^0 \to ee\gamma$ decays. In the calculation for these two decays the number of events generated was normalized to the number of $K_L^0 \to \pi^+\pi^-$ events. The correction for the misidentification, $\pi \to e$, was $(1.31 \pm 0.08) \times 10^{-4}$, which was calculated by averaging the particle identification efficiencies over the acceptance of the $K_L^0 \to \pi e \nu$ decay. The $K_L^0 \to ee\gamma$ events were gen-

erated using the equations given by Bergström *et al.* [26], in which the parameter $\alpha_{K^*} = -0.28^{+0.082}_{-0.079}$ quoted from two previous experiments [27,28] was used. In the low mass region the distribution was well reproduced by the calculation. However, it suggested the presence of contributions from other sources above 470 MeV/c^2. The contribution from the $K_L^0 \to e^+e^-e^+e^-$ decay was calculated using the equations given by Miyazaki and Takasugi [29] based on the double internal conversion process of the Knoll-Wada formula [30]. The validity of this formula was confirmed by Samios *et al.* [31] for a similar decay, $\pi^0 \to e^+e^-e^+e^-$.

Figure 42 is a scatter plot of e^+e^- events obtained by a Monte Carlo calculation which included the $K_L^0 \to \pi e \nu$, $ee\gamma$, and $e^+e^-e^+e^-$ decays at a ten times the sensitivity of the experiment. The general shape of the Monte Carlo generated distribution is quite similar to the distribution of the actual data. The high mass events were explained by the sum of the contributions from the $K_L^0 \to ee\gamma$ and $K_L^0 \to e^+e^-e^+e^-$ decays.

The expected number of the background events in the $K_L^0 \to ee$ fiducial region was 0.1 The one event in the fiducial region for the $K_L^0 \to ee$ decay cannot be distinguished from the contribution due to the high mass tail of the $M_{e^+e^-}$ distributions from the $K_L^0 \to ee\gamma$ and $K_L^0 \to e^+e^-e^+e^-$ decays at the level of our experimental sensitivity. Therefore, we set an upper limit on the branching ratios of $K_L^0 \to ee$ as $B(K_L^0 \to ee) < 1.6 \times 10^{-10}$ at 90% confidence level which corresponded to the 3.9 event sensitivity.

D. $K_L^0 \to e^+e^-e^+e^-$

There were 18 and 6 events in the regions $M_{e^+e^-} > 470$ MeV/c^2 and $M_{e^+e^-} > 480$ MeV/c^2, respectively. No event was expected from the $K_L^0 \to \pi e \nu$ decay there.
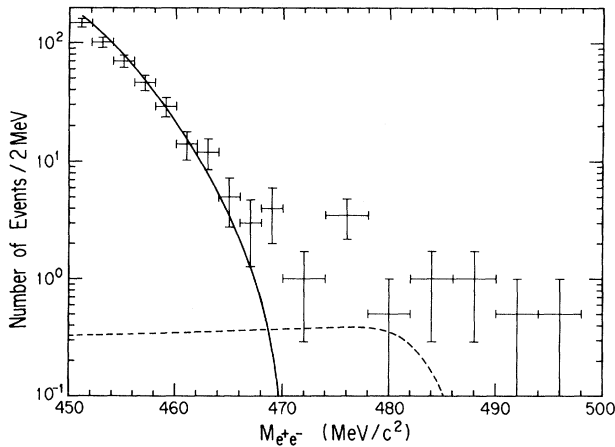

FIG. 41. $M_{e^+e^-}$ distribution for events with $P_t < 20$ MeV/c. The solid and dotted curves show the contributions from the $K_L^0 \to \pi e \nu$ and $K_L^0 \to ee\gamma$ decays, respectively. These curves are the results of Monte Carlo calculations normalized to the observed number of $K_L^0 \to \pi^+\pi^-$ events.
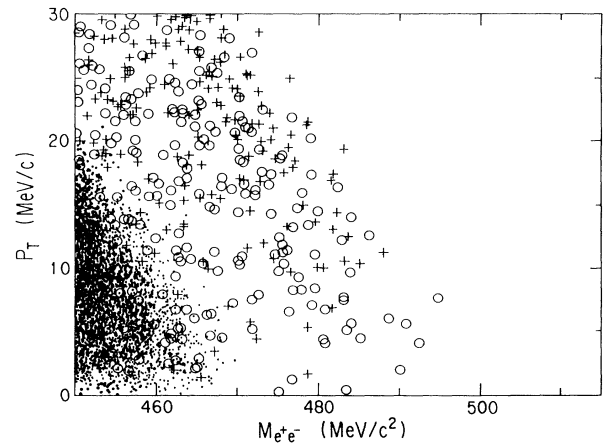

FIG. 42. Monte Carlo generated $M_{e^+e^-}$ vs P_t plot with ten times the sensitivity of the experiment. The dots indicate events from the $K_L^0 \to \pi e \nu$ decay, the crosses those from the $K_L^0 \to ee\gamma$ decay, and the open circles those from the $K_L^0 \to e^+e^-e^+e^-$ decay.

The numbers of events expected from the $K_L^0 \to ee\gamma$ decay were 4.4 ± 0.9 and 0.8 ± 0.2 in those two regions, respectively. These values together with their errors were obtained by using the averaged value of the branching ratios obtained by the two previous experiments [27,28]. Another possible source of these events is the external conversion of γ's from the $K_L^0 \to ee\gamma$ and $K_L^0 \to \gamma\gamma$ decays. The numbers of events expected in the regions $M_{e^+e^-} > 470$ MeV/c^2 and $M_{e^+e^-} > 480$ MeV/c^2 from external conversion was estimated by a cascade shower calculation to be 0.45 and 0.20 events from the $K_L^0 \to ee\gamma$ decay and 0.19 and 0.06 events from the $K_L^0 \to \gamma\gamma$ decay. The smallness of the contributions from the external conversion was due to the small thickness of the material in the spectrometer region. The distribution of the closest distance between two tracks, D_{vertex}, for these 18 events is shown in Fig. 43. It is similar to that for the $K_L^0 \to \pi^+\pi^-$ decay. The background from the double misidentification of a pair of hadrons, which were produced in the decay chamber by the interaction of the neutral beam with the residual gas, was estimated to be at most 0.01 event in the region $M_{e^+e^-} > 470$ MeV/c^2.

After subtracting the background contributions from the $K_L^0 \to ee\gamma$ decay and external conversion we estimated the branching ratio of the $K_L^0 \to e^+e^-e^+e^-$ to be $(6 \pm 2 \pm 1) \times 10^{-8}$ using 18 events in the region $M_{e^+e^-} > 470$ MeV/c^2, and $(7 \pm 3 \pm 2) \times 10^{-8}$ using 6 events in the region $M_{e^+e^-} > 480$ MeV/c^2. The first error is statistical and the second systematic. The systematic error was estimated by the quadratic sum of the following errors. There were 3 and 5 % uncertainties in the acceptance calculation and 8 and 7 % uncertainties in the background subtraction in the regions $M_{e^+e^-} > 470$ MeV/c^2 and $M_{e^+e^-} > 480$ MeV/c^2, and 1% uncertainty in particle identification for both regions. In the fiducial region for the $K_L^0 \to ee$ decay, about 0.1 event was expected from the $K_L^0 \to ee$ decay assuming the branching ratio given by the standard model. Therefore, the one event in the $K_L^0 \to ee$ fiducial region was included
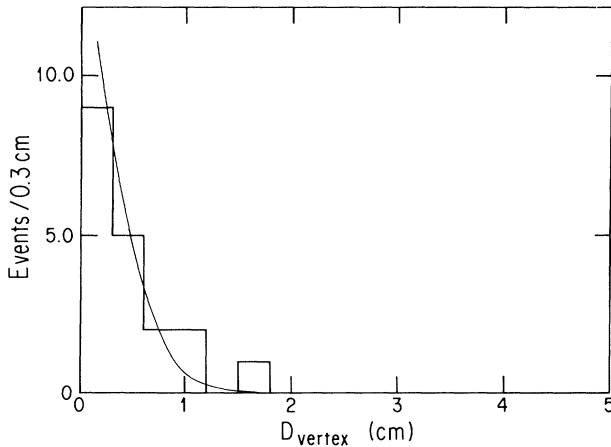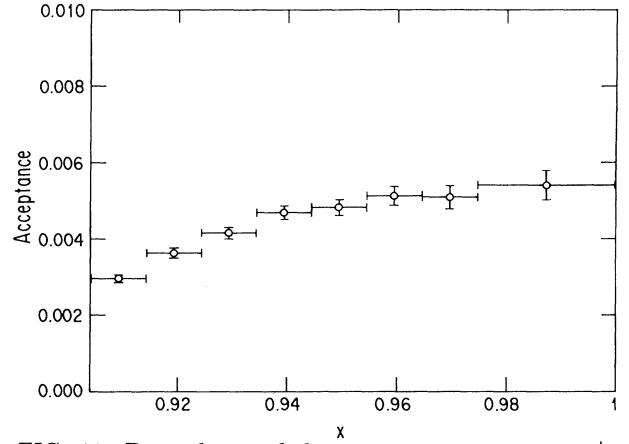

FIG. 44. Dependence of the acceptance on x, the e^+e^- mass divided by the K_L^0 mass $(M_{e^+e^-}/M_{K_L^0})$.

in the systematic uncertainty for the estimation of the branching ratio of the $K_L^0 \to e^+e^-e^+e^-$ decay. Figure 44 shows the dependence of the acceptance on $M_{e^+e^-}$ which would be important for the theoretical analysis of the decay process, particularly for the study of the form factor.

E. $K_L^0 \to \mu\mu$

Figure 45 shows a scatter plot of $M_{\mu\mu}$ vs θ^2 for the $\mu\mu$ events. Figures 46(a) and 46(b) are an $M_{\mu\mu}$ distribution for which $\theta^2 < 3$ mrad^2, and a θ^2 distribution in the region $493 < M_{\mu\mu} < 502$ MeV/c^2. A peak centered at the K_L^0 mass and $\theta^2 = 0$ mrad^2 is clearly separated from the background and a Monte Carlo calculation well reproduces both distributions.

The background seen in the region $M_{\mu\mu} < 490$ MeV/c^2 was explained by two sources from the $K_L^0 \to \pi\mu\nu$ decay in the same way as done for the $K_L^0 \to \mu e$ mode. One was

FIG. 43. Distribution of the distance between two tracks (D_{vertex}) for the e^+e^- events with $M_{e^+e^-} > 470$ MeV/c^2. The solid curve shows the D_{vertex} distribution for the $K_L^0 \to \pi^+\pi^-$ events.
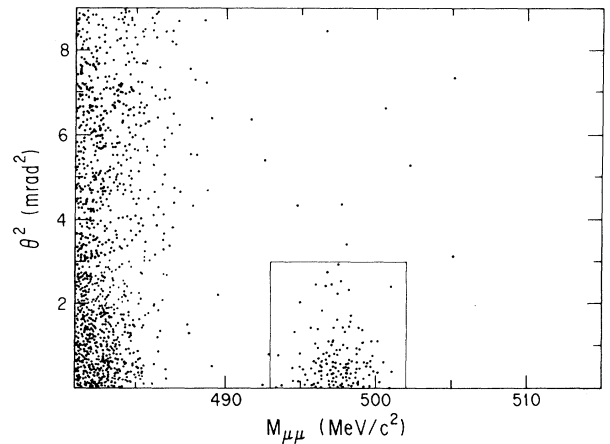

FIG. 45. Scatter plot of $M_{\mu\mu}$ vs θ^2 for the $\mu\mu$ events. The box represents the boundary of the fiducial region.
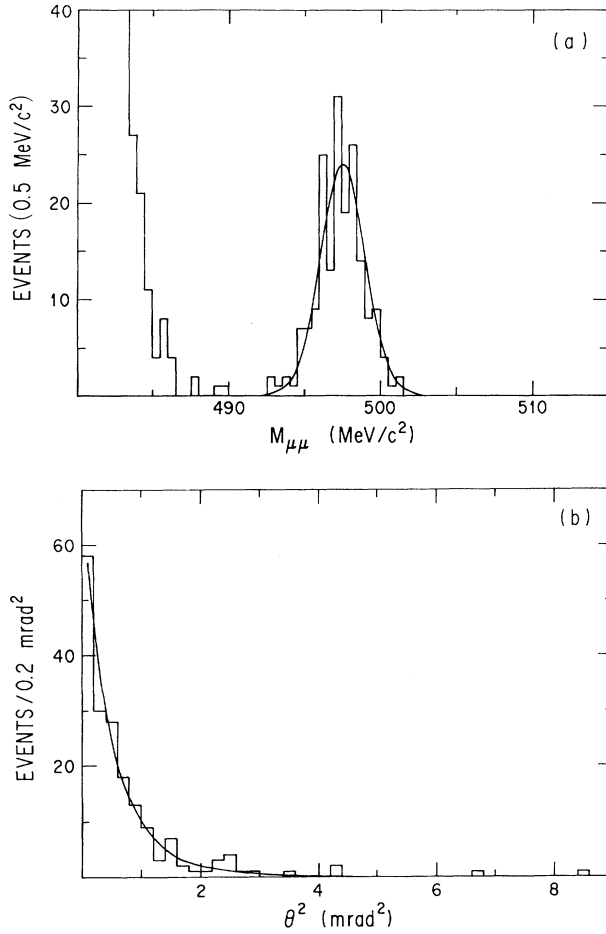
FIG. 46. Distributions of (a) $M_{\mu\mu}$ with $\theta^2 < 3$ (mrad)^2 and (b) θ^2 with $493 < M_{\mu\mu} < 502$ MeV/c^2 for the $\mu\mu$ events. The solid lines are the distributions of Monte Carlo generated $K_L^0 \to \mu\mu$ events normalized to contain the same number of events in the fiducial region.

FIG. 47. Scatter plots of $M_{\mu\mu}$ vs θ^2 in an extended mass region for (a) the events collected in the first running period of $0°$ production and (b) those in the second running period of $2°$ production. The box shows the boundary for the $K_L^0 \to \mu\mu$ fiducial region.

due to $\pi \to \mu$ misidentification and the other due to the $\pi \to \mu\nu$ decay in the decay chamber. The background above 490 MeV/c^2 was due to the decay in flight in the spectrometer of the pion from the $K_L^0 \to \pi\mu\nu$ decay and to the double misidentification of both the pion and the electron from the $K_L^0 \to \pi e \nu$ decay as muons. The numbers of events expected from these two sources were 1.5 and 0.7 in the region $M_{\mu\mu} > 490$ MeV/c^2 and $4 < \theta^2 < 9$ mrad^2, respectively. These numbers should be compared with 17 real events in the same region in Figs. 47(a) and 47(b). The source for the excess was thought to be pairs of hadrons which were produced by the interactions of neutral particles in the beam with the residual gas in the decay chamber for the following reasons. There were several real events beyond the mass of 520 MeV/c^2, which was the maximum value of the $\mu\mu$ mass in the case of double misidentification of the $K_L^0 \to \pi e \nu$ decay. The number of events in this mass region for the $0°$ run was much larger than that for the $2°$ run, while the sensitivities for both runs were comparable. The ratio of the numbers of events in the region $M_{\mu\mu} > 490$ MeV/c^2 and
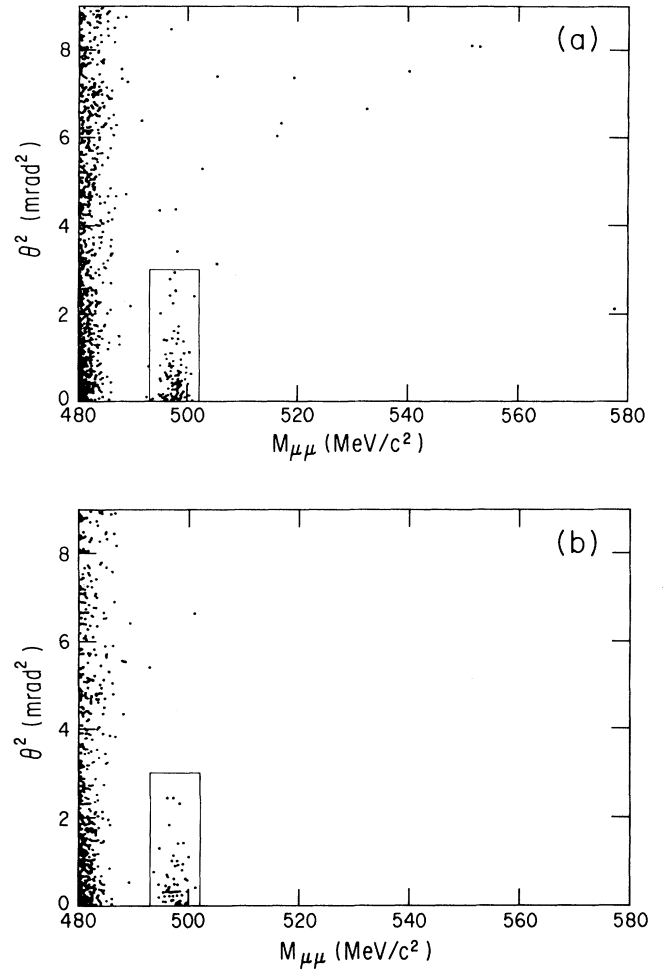
$4 < \theta^2 < 9$ mrad^2 from the $0°$ and $2°$ runs was $15/2$, and the ratio of the interaction probabilities for the two runs, which were estimated by the product of the fraction of neutrons in the beam, the vacuum pressure in the decay chamber and the running time, was about $9/1$. These two values are consistent with each other.

The number of $\mu\mu$ events in the fiducial region was 179. Assuming a flat background over θ^2, we considered the region bounded by $493 < M_{\mu\mu} < 502$ MeV/c^2 and $3 < \theta^2 < 9$ mrad^2 as a control region. The number of $\mu\mu$ events in the control region was 5, and the number of real $\mu\mu$ events in the same region was expected to be 2.6 from the Monte Carlo calculation. Therefore, the number of background $\mu\mu$ events in the fiducial region was estimated to be 1.2 $[(5 - 2.6)/2 = 1.2)]$. After subtracting it the number of $K_L^0 \to \mu\mu$ events in the fiducial region became $177.8 \pm 1.34(\text{stat}) \pm 1.2(\text{syst})$, where the systematic error was the number of the subtracted events. The branching ratio of the $K_L^0 \to \mu\mu$ decay was then calculated using the single-event sensitivity to be

TABLE III. Results of the $K_L^0 \to \mu\mu$ branching ratio obtained for different muon identification processes. $\circ$ means that the identifier information was used and $\times$ means that it was not. $N_{\mu\mu}$ was obtained from the relation $N_{\mu\mu} = N_{\mu\mu}^0 - (N_{\mu\mu}^{\rm BG}/2 - 1.2)$ as described in the text except for the third column (the second identification process). In the third column either of the electron identifiers were not used, and the main background source is the $K_L^0 \to \pi e \nu$ decay. Therefore, $N_{\mu\mu}$ in the third column was estimated by subtracting from $N_{\mu\mu}^0$ a Monte Carlo calculated number of 24.4 which was expected in the fiducial region from the double misidentification of the pion and electron from the $K_L^0 \to \pi e \nu$ decay as muons. The uncertainties of the branching ratios are statistical.

| Muon identifier | $\circ$ | $\circ$ | $\times$ | $\circ$ | $\circ$ |
| Cherenkov | $\circ$ | $\times$ | $\circ$ | $\circ$ | $\times$ |
shower counter	$\circ$	$\times$	$\circ$	$\times$	$\circ$
$N_{\mu\mu}^0$	179	215	185	190	179
$N_{\mu\mu}^{\rm BG}$	5	39	11	7	5
$N_{\mu\mu}$	177.8	190.6	180.8	187.8	177.8
$\epsilon({\rm PID})_{\mu\mu}$	0.763	0.799	0.790	0.796	0.766
$N_{\mu\mu}/\epsilon({\rm PID})_{\mu\mu}$	233.0	238.6	228.9	236.1	232.2
$10^9 B(K_L^0 \to \mu\mu)$	$(7.9 \pm 0.6) \times 10^{-9}$	$(8.1 \pm 0.6) \times 10^{-9}$	$(7.7 \pm 0.6) \times 10^{-9}$	$(8.0 \pm 0.6) \times 10^{-9}$	$(7.9 \pm 0.6) \times 10^{-9}$

$[7.9 \pm 0.6(\text{stat})\pm 0.2(\text{syst})] \times 10^{-9}$.

The reliability of the above value of the branching ratio was verified by the following checks. The difference in the branching ratio value between the two running periods was within the error. Using the $K_L^0 \to \pi^+\pi^-$ sample obtained by requiring the parallel trigger coincidence for the hodoscopes in an off-line analysis the value of the branching ratio changed to $(8.0 \pm 0.6) \times 10^{-9}$ which was consistent within the systematic error. The branching ratios were calculated separately in three K_L^0 momentum regions, and they were consistent with each other within the errors. The branching ratio was calculated by changing the particle identification process as summarized in Table III. The resultant values were all consistent with the value obtained by the process used in our analysis within the systematic error.

V. SUMMARY AND DISCUSSIONS

We have performed a high-sensitivity search for the $K_L^0 \to \mu e$ and ee decays, and a precise measurement of the branching ratio of the $K_L^0 \to \mu\mu$ decay. The upper limits for the branching ratios of the $K_L^0 \to \mu e$ and ee decays were 9.4×10^{-11} and 1.6×10^{-10} at 90% confidence level, respectively. The branching ratio of the $K_L^0 \to \mu\mu$ decay was $[7.9 \pm 0.6(\text{stat})\pm 0.2(\text{syst})] \times 10^{-9}$. The branching ratio of the $K_L^0 \to e^+e^-e^+e^-$ decay was estimated from the e^+e^- sample to be

$$B(K_L^0 \to e^+e^-e^+e^-) = [6 \pm 2(\text{stat}) \pm 1(\text{syst})] \times 10^{-8}$$

for $M_{e^+e^-} > 470$ MeV/c^2 and $[7\pm3(\text{stat})\pm2(\text{syst})]\times10^{-8}$ for $M_{e^+e^-} > 480$ MeV/c^2.

The upper limit for the $K_L^0 \to \mu e$ decay has been significantly improved by E791 at BNL [14] and our experiment over the previous value of 1.9×10^{-9} [11]. The present value gives a lower limit of about 100 TeV/c^2 for

the mass of the horizontal gauge boson. Most models, which are based on a naive model of the extended technicolor, can be excluded by the present result, because they predict the branching ratio of the $K_L^0 \to \mu e$ decay to be around the previous experimental limit. Although the rare muon decays [32] involving a lepton-flavor-changing process will give a more stringent limit for some models, the $K_L^0 \to \mu e$ decay is complementary to them, because the generation number is conserved in the kaon decays but not in the muon decays. The lepton-flavor-changing kaon decay, $K^+ \to \pi \mu e$ [33], is complementary to the $K_L^0 \to \mu e$ decay. The former probes a scalar or vector interaction and the latter a pseudoscalar or axial-vector interaction.

The most serious source of the background for the $K_L^0 \to \mu e$ decay was the decay in flight in the spectrometer of the pion from the $K_L^0 \to \pi e \nu$ decay followed by a mismeasurement of the track momentum due to accidental hits in the drift chambers and hodoscopes. In order to reduce this background a more redundant measurement of the tracks should be made in future experiments with higher sensitivities.

The upper limit for the $K_L^0 \to ee$ decay was also improved by E791 [14] and by us over the previous value of 1.2×10^{-9} [12]. The unexplored branching ratio region up to the value predicted by the standard model, $(3\text{--}5)\times10^{-12}$, has been narrowed considerably by the present upper limit. It sets a good constraint on models which can avoid helicity suppression. In the search for the $K_L^0 \to ee$ decay we have found that the main background comes from the $K_L^0 \to e^+e^-e^+e^-$ decay and estimated its branching ratio using high e^+e^- mass events. The present value of the branching ratio of the $K_L^0 \to e^+e^-e^+e^-$ decay is consistent with the previous ones: $(4\pm3) \times 10^{-8}$ by Barr et al. [34] based on 2 events and $(3.07\pm1.25\pm0.26) \times 10^{-8}$ by Vagins et al. [35] based on 6 events, and is also consistent with the recent value of $(3.96 \pm 0.78 \pm 0.32) \times 10^{-8}$ by Gu et al. [36] based on

27 events. All these data by other groups were obtained from measurement of the four-electron final state, and the mass of each e^+e^- pair is not so large as the present one.

The $K_L^0 \to e^+e^-e^+e^-$ decay would be more useful for an estimation of the long-distance effect in the $K_L^0 \to \mu\mu$ decay than the $K_L^0 \to ee\gamma$ decay currently used [37]. The form-factor effect, which is important for the estimation of the long-distance effect, would be large in the high $M_{e^+e^-}$ region which was covered by the present experiment. The flat dependence of our detection acceptance on $M_{e^+e^-}$ will provide useful information for the form factor analysis.

The time-ordered plot of the measured branching ratio of the $K_L^0 \to \mu\mu$ decay is shown in Fig. 48 together with the unitarity limit. The present value is larger than the unitarity bound even though it is statistically consistent with it. If we use our value, we could estimate that the top-quark mass should be less than 280 GeV/c^2. However, the top quark mass value depends on theoretical models [37,39–41] used in the estimation of the long-distance effect. We expect that such theoretical ambiguity will be reduced in future by an extensive study of the long-distance effect using more abundant data of the decays $K_L^0 \to ee\gamma$, $K_L^0 \to \mu\mu\gamma$, $K_L^0 \to e^+e^-e^+e^-$, and $\eta \to \mu\mu$.
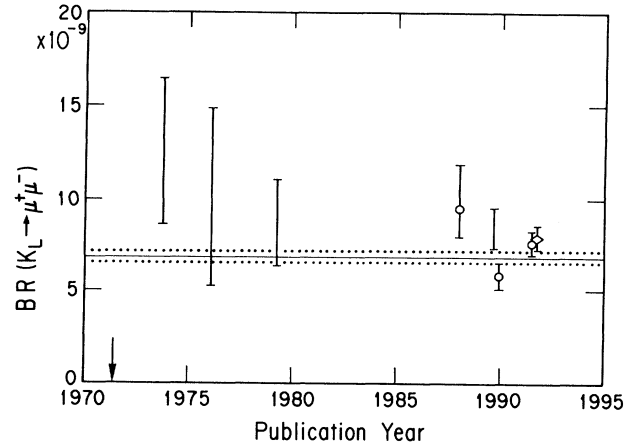

FIG. 48. Time-ordered plot of the $K_L^0 \to \mu\mu$ branching ratios obtained by all experiments up to the present time. The horizontal lines show the unitarity limit and its allowed range; the solid line shows its mean value and the dotted lines show its allowed range due to the experimental uncertainty of the $K_L^0 \to \gamma\gamma$ branching ratio. The diamond with an error bar is the result of the present experiment. The results by the BNL-E791 Collaboration [14] are shown by the circles with error bars and the others [13] are shown by the bars. The arrow shows the upper limit (90% C.L.) by Clark *et al.* [11].

[1] P. Langacker, S. U. Sankar, and K. Schilcher, Phys. Rev. D **38**, 2841 (1988).

[2] W. S. Hou and A. Soni, Phys. Rev. Lett. **54**, 2083 (1985).

[3] A. Barroso, G. C. Branco, and M. C. Bento, Phys. Lett. **134B**, 123 (1984).

[4] J. C. Pati and H. Stremnizer, Phys. Lett. B **172**, 441 (1986).

[5] J. Ellis, D. V. Nanopoulos, and P. Sikivie, Phys. Lett. **101B**, 387 (1981); S. Dimopoulos, S. Raby, and G. L. Kane, Nucl. Phys. **B182**, 77 (1981); E. Eichten, I. Hinchliffe, K. D. Lane, and C. Quigg, Phys. Rev. D **34**, 1547 (1986).

[6] L. M. Sehgal, Phys. Rev. **183**, 1511 (1969); Phys. Rev. D **4**, 1582(E) (1971).

[7] G. L. Kane and R. E. Shrock, in *Intense Medium Energy Sources of Strangeness*, edited by T. Goldman, H. E. Haber, and H. F. W. Sadrozinski, AIP Conf. Proc. No. 102 (AIP, New York, 1983), p. 123.

[8] B. R. Martin, E. de Rafael, and J. Smith, Phys. Rev. D **2**, 179 (1970).

[9] Particle Data Group, K. Hikasa *et al.*, Phys. Rev. D **45**, S1 (1992).

[10] S. L. Glashow, J. Iliopoulos, and L. Maiani, Phys. Rev. D **2**, 1285 (1970); M. Kobayashi and T. Maskawa, Prog. Theor. Phys. **49**, 652 (1973); M. K. Gaillard and B. W. Lee, Phys. Rev. D **10**, 897 (1974); M. K. Gaillard, B. W. Lee, and R. E. Shrock, *ibid.* **13**, 2674 (1976); R. E. Shrock and M. B. Voloshin, Phys. Lett. **87B**, 375 (1979); T. Inami and C. S. Lim, Prog. Theor. Phys. **65**, 297 (1981); **65**, 1772(E) (1981); A. J. Buras and M. K. Harlander, in *Heavy Flavors*, edited by A. J. Buras and M. Lindner (World Scientific, Singapore, 1992).

[11] A. R. Clark *et al.*, Phys. Rev. Lett. **26**, 1667 (1971); H. B. Greenlee *et al.*, *ibid.* **60**, 893 (1988); S. F. Schaffner *et al.*, Phys. Rev. D **39**, 990 (1989).

[12] E. Jastrzembski *et al.*, Phys. Rev. Lett. **61**, 2300 (1988).

[13] W. C. Carithers *et al.*, Phys. Rev. Lett. **30**, 1336 (1973); **31**, 1025 (1973); Y. Fukushima *et al.*, *ibid.* **36**, 348 (1976); M. J. Shochet *et al.*, Phys. Rev. D **19**, 1965 (1979).

[14] R. D. Cousins *et al.*, Phys. Rev. D **38**, 2914 (1988); C. Mathiazhagan *et al.*, Phys. Rev. Lett. **63**, 2181 (1989); A. P. Heinson *et al.*, Phys. Rev. D **44**, R1 (1991); K. Arisaka *et al.*, Phys. Rev. Lett. **70**, 1049 (1993); K. Arisaka *et al.*, *ibid.* **71**, 3910 (1993).

[15] T. Inagaki *et al.*, Phys. Rev. D **40**, 1712 (1989); T. Akagi *et al.*, Phys. Rev. Lett. **67**, 2614 (1991); T. Akagi *et al.*, *ibid.* **67**, 2618 (1991); T. Akagi *et al.*, Phys. Rev. D **47**, R2644 (1993).

[16] J. R. Sanford and C. L. Wang, BNL Report No. 11279, 1967 (unpublished); BNL Report No. 11479, 1967 (unpublished).

[17] T. K. Ohska *et al.*, KEK Report No. 85-10, 1985 (unpublished); IEEE Trans. Nucl. Sci. **33**, 98 (1986).

[18] H. Wind, Nucl. Instrum. Methods **115**, 431 (1974).

[19] R. K. Bock, H. Grote, D. Notz, and M. Regler, *Data Analysis Techniques for High Energy Physics Experiment* (Cambridge University Press, Cambridge, 1990).

[20] W. R. Nelson, H. Hirayama, and D. W. O. Rogers, SLAC Report No. 265, 1985 (unpublished).

[21] J. B. Marion and B. A. Zimmerman, Nucl. Instrum. Methods **51**, 93 (1967).

[22] The Monte Carlo events for the decay $K_L^0 \to \pi^+\pi^-\gamma$ were generated using the theoretical formula cited in Ref. [23] and the experimental branching ratio by A. Carroll *et al.* [Phys. Rev. Lett. **44**, 529 (1980)]. The extrapolation of the minimum photon energy from the experimental value of 20–0.5 MeV and the correction for the branching ratio of the decay $K_L^0 \to \pi^+\pi^-$ were performed by a calculation of the radiative correction under the guidance of Y. Shimizu. The recent improved data of the decay $K_L^0 \to \pi^+\pi^-\gamma$ by E. J. Ramberg *et al.* [*ibid.* **70**, 2525 (1993)] was consistent with that by A. Carroll *et al.*

[23] B. deWitt and J. Smith, *Field Theory in Particle Physics* (North-Holland, Amsterdam, 1986), Vol. 1.

[24] P. A. Aarnio, J. Ranft, and G. R. Stevenson, CERN Report No. TIS-RP/106-Rev, 1984 (unpublished).

[25] R. D. Cousins and V. L. Highland, Nucl. Instrum. Methods Phys. Res. Sect. A **320**, 331 (1992).

[26] L. Bergström, E. Massó, and P. Singer, Phys. Lett. **131B**, 229 (1983).

[27] K. E. Ohl *et al.*, Phys. Rev. Lett. **65**, 1407 (1990).

[28] G. D. Barr *et al.*, Phys. Lett. B **240**, 283 (1990).

[29] T. Miyazaki and E. Takasugi, Phys. Rev. D **8**, 2051 (1973).

[30] N. M. Knoll and W. Wada, Phys. Rev. **98**, 1355 (1955).

[31] N. P. Samios *et al.*, Phys. Rev. **126**, 1844 (1962).

[32] R. D. Bolton *et al.*, Phys. Rev. D **38**, 2077 (1988); U. Bellgardt *et al.*, Nucl. Phys. **B299**, 1 (1988); S. Ahmad *et al.*, Phys. Rev. D **38**, 2102 (1988).

[33] A. M. Lee *et al.*, Phys. Rev. Lett. **64**, 165 (1990).

[34] G. D. Barr *et al.*, Phys. Lett. B **259**, 389 (1991).

[35] M. R. Vagins *et al.*, Phys. Rev. Lett. **71**, 35 (1993).

[36] P. Gu *et al.*, Phys. Rev. Lett. **72**, 3000 (1994).

[37] L. Bergström, E. Massó, and P. Singer, Phys. Lett. B **249**, 141 (1990).

[38] The $K_L^0 \to \mu\mu$ decay amplitude $A_{\mu\mu}$ was divided into real and imaginary parts $|A_{\mu\mu}|^2 + |\mathrm{Re}A_{\mu\mu}|^2 + |\mathrm{Im}A_{\mu\mu}|^2$. The imaginary part $\mathrm{Im}A_{\mu\mu}$ was calculated by using the data of $B(K_L^0 \to \gamma\gamma)$ land the standard QED calculation. The real part was expressed by the summation $\mathrm{Re}A_{\mu\mu} = A_{\mathrm{EM}} + A_W$, where A_{EM} is the long-distance part from the 2γ exchange diagram and A_W is the short-distance part from the Z^0 exchange and W box diagrams. For the estimation of A_{EM} we used the theoretical analysis given by Bergström *et al.* [37]. Finally the upper limit of the top mass was obtained from the one-standard deviation of the present $K_L^0 \to \mu\mu$ result.

[39] Bélanger and C. Q. Geng, Phys. Rev. D **43**, 140 (1991).

[40] C. Q. Geng and J. N. Ng, Phys. Rev. D **41**, 2351 (1990).

[41] V. Barger, W. F. Long, E. Ma, and A. Pramudita, Phys. Rev. D **25**, 1860 (1982).